Graphical Abstract

A three-dimensional micropolar beam model with application to the finite deformation analysis of hard-magnetic soft beams

Farzam Dadgar-Rad,Amirreza Hemmati,Mokarram Hossain

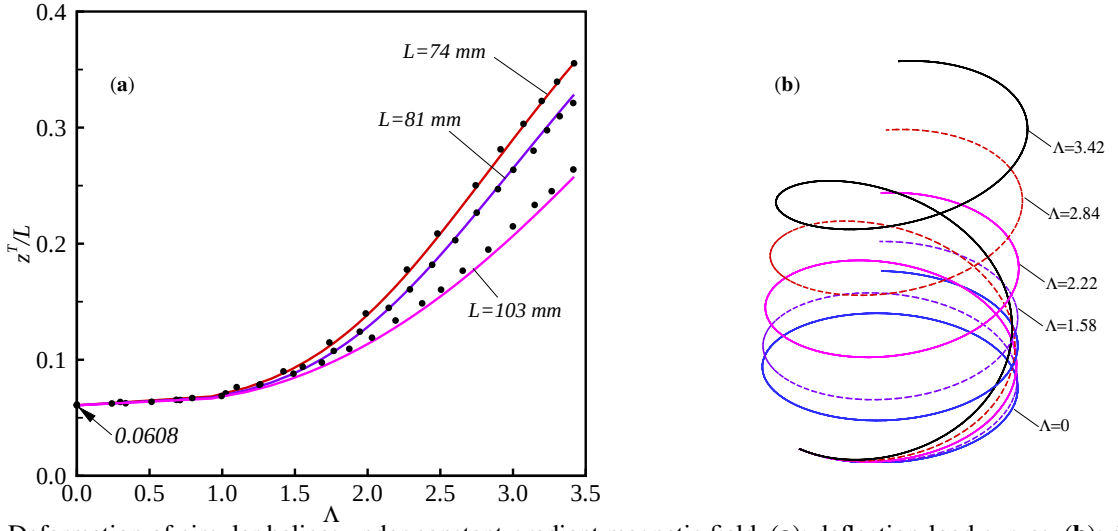

Deformation of circular helices under constant-gradient magnetic field, (**a**): deflection-load curves, (**b**): deformed shapes in the 3d space for the helix with $L = 103$ mm and $\Lambda \in \{1.58, 2.22, 2.84, 3.42\}$

In this example, large deformation of three circular helices having the total lengths $L = 74$, 81, and 103 (mm), and subjected to a constant-gradient magnetic field is simulated. If the coordinate line X_3 is along the helix axis, the undeformed geometry is described by $X_1 = R\cos\alpha$, $X_2 = R\sin\alpha$, and $X_3 = K\alpha$, with $K = \frac{p}{2\pi}$. Here, α is the polar angle, R is the initial radius, and p is the initial pitch of the helix. In all cases, the helix radius, the wire diameter, and the helix angle are, respectively, considered to be $R = 10$, $d = 2$ (mm), and $\eta = 1.51$ rad. The effective Young modulus is $E = 1.32$ (MPa), and the micropolar parameters are considered to be $\eta = 0.1\mu$ and $l = 0.1h$. The remnant magnetic field is directed along the X_3 axis, and its magnitude, in the three helices is $\tilde{B}^{\text{rem}} = 13$, 26 and 13 (mT), respectively. Moreover, the constant-gradient magnetic loading is of the form $\mathbb{B}^{\text{ext}} = -\frac{1}{2}b(x_1\mathbb{e}_1 + x_2\mathbb{e}_2 - 2x_3\mathbb{e}_3)$ where b is the intensity of the magnetic field per unit length. The nondimensional tip position z^T/L along the x_3-axis vs the nondimensional loading parameter $\Lambda = L(Zb)^{1/3}$, with $Z = A\tilde{B}^{\text{rem}}/(\mu_0 EI)$, is displayed in the left panel of the figure. The results based on the present micopolar beam formulation are in good agreement with the data reported by Sano et al. (2022). Moreover, the three-dimensional deformed shapes of the helix with $L = 103$ (mm) for for several values of the loading parameter Λ are demonstrated in the right panel of the figure.

Highlights

A three-dimensional micropolar beam model with application to the finite deformation analysis of hard-magnetic soft beams

Farzam Dadgar-Rad,Amirreza Hemmati,Mokarram Hossain

- A 3D beam model based upon the micropolar theory is developed.
- A nonlinear FE formulation for the present beam model is elaborated.
- Both size effect and magnetic loading can be modeled by the present formulation.
- Numerical results reveal the good performance of the present formulation.

A three-dimensional micropolar beam model with application to the finite deformation analysis of hard-magnetic soft beams

Farzam Dadgar-Rad[a,*], Amirreza Hemmati[a] and Mokarram Hossain[b]

[a]Faculty of Mechanical Engineering, University of Guilan, Rasht, 695013, Guilan, Iran
[b]Zienkiewicz Institute for Modelling, Data and AI, Faculty of Science and Engineering, Swansea University, SA1 8EN, UK

ARTICLE INFO

Keywords:
Micropolar continuum
3D beam
Hard-magnetic soft materials
Magneto-elasticity
Finite element method

ABSTRACT

The main purpose of this contribution is to develop a three-dimensional (3D) nonlinear beam model based on the micropolar continuum theory. To do so, a kinematic model based on the deformation of three directors and accounting for the micro-rotation tensor of the micropolar theory is introduced. One of the main characteristics of the present beam model is that 3D constitutive equations without any modification can be directly used in the formulation. Furthermore, it is known that a body couple field is induced in hard-magnetic soft materials (HMSMs) when subjected to external magnetic fluxes. Therefore, the stress tensor in HMSMs is asymmetric, in general. Since the asymmetry of stress is one of the main features of the micropolar theory, the present formulation can be used for analyzing the deformation of beams made of HMSMs. Accordingly, the virtual external work of the present model is formulated so that it accounts for the contribution from uniform or constant-gradient external magnetic fluxes on the beam. Moreover, a Total Lagrangian (TL) nonlinear finite element (FE) formulation to provide numerical solutions of the related problems is developed. Several numerical examples are solved to investigate the capability of the developed formulation. It is shown that the present formulation can model the size-dependent behavior of beam-like structures if the material length-scale parameter of the micropolar constitutive model is comparable to the thickness of the beam. Moreover, the proposed model can successfully predict the finite deformation of 3D beams made of HMSMs subjected to magnetic loading.

1. Introduction

It has been proven experimentally that the classical continuum theory cannot predict the size-dependent behavior of materials at micron scales (e.g., Lam et al. (2003); McFarland and Colton (2005); Voyiadjis and Song (2019)). Moreover, it cannot be employed for the cases where the material particles are subjected to body couples (e.g., Truesdell and Noll (2004)). Moreover, generalized continuum models including gradient-based (Mindlin, 1965), micromorphic (Eringen, 1966), micropolar (Kafadar and Eringen, 1971), and non-local (Eringen and Edelen, 1972) theories have been developed in the 20th century that involve material length-scale parameters and can be used in situations were the classical continuum theory fails to predict the behavior of materials. Among them, the micropolar continuum theory is a successful approach that can take both size-effect and body couple into account. Therefore, in this work, it has been employed as the fundamental continuum model to develop a 3D beam formulation.

The basic mathematical formulation of the micropolar continuum theory has been developed by Eringen and his coworkers (e.g., Kafadar and Eringen (1971); Eringen and Kafadar (1976); Eringen (1999)). In this theory, it is assumed

*Corresponding author
dadgar@guilan.ac.ir (F. Dadgar-Rad); hemmati_amirreza@yahoo.com (A. Hemmati); mokarram.hossain@swansea.ac.uk (M. Hossain)
ORCID(s): 0000-0003-1546-2446 (F. Dadgar-Rad); 0000-0001-0000-0000 (A. Hemmati); 0000-0002-4616-1104 (M. Hossain)

that there exists a micro-structure inside each macro-element that experiences rigid rotation independently from the macro-displacement of its surrounding macro-element. It has been shown that the micropolar elasticity is able to predict the size-dependent finite elastic deformation of solids (e.g., Ramezani et al. (2008, 2009b); Bauer et al. (2010, 2012a); Erdelj et al. (2020)). Extensions of micropolar theory to elasto-plasticity, for the purpose of modelling the strain localization phenomenon in plastic deformations, have been carried out in several research papers (e.g., de Borst (1993); Steinmann (1994); Grammenoudis and Tsakmakis (2007); Grammenoudis et al. (2007); Bauer et al. (2012b)). Various micropolar beam (Ramezani et al., 2009a; Hassanpour and Heppler, 2016; Chowdhury and Reddy, 2019; Obrezkov et al., 2022; Sargsyan and Khachatryan, 2022; La Valle and Falsone, 2023), plate (Abadikhah and Folkow, 2015; Fares et al., 2023), and shell (Eremeyev and Altenbach, 2017; Zozulya, 2018) formulations have been also developed in the literature. Additionally, the micropolar theory has been used in the modeling of granular materials, phononic crystals, lattice structures, crystal plasticity, bone mechanics, and auxetic lattices (e.g., Mayeur et al. (2011); Spadoni and Ruzzene (2012); Goda et al. (2014); Yoder et al. (2018); Guarín-Zapata et al. (2020); Cui et al. (2023); Tian et al. (2023)). Furthermore, micropolar formulations of phase-field fracture mechanics and peridynamic theory have been also proposed in modeling the fracture-based engineering problems (e.g., Suh et al. (2020); Wan et al. (2022)).

As was mentioned above, micropolar theory can model the deformation of materials subjected to body couples. A class of newly invented smart materials, known as *hard-magnetic soft materials* or HMSMs, experience body couples under external magnetic stimuli. HMSMs are composed of inherently magnetic particles with high coercivity, e.g., NdFeB or $CoFe_2O_4$, so that their magnetization vector remains unchanged even for large values of external magnetic loading (e.g., Bastola and Hossain (2021); Lucarini et al. (2022)). Interaction between the internal magnetization vector and external magnetic loading induces a body couple in HMSMs (Dorfmann and Ogden, 2014; Zhao et al., 2019; Wang et al., 2020). Consequently, the Cauchy stress tensor in HMSMs is naturally asymmetric, and micropolar theory is a candidate for mathematical modeling of these materials. HMSMs are employed as soft robots, sensors, soft and flexible electronics, actuators, vibration absorbers, and isolators (see, e.g., Kim et al. (2018); Ren et al. (2019); Wu et al. (2020); Kuang et al. (2019); Wang et al. (2021); Wu et al. (2021); Saber and Sedaghati (2023)). Various continuum-based (e.g., Zhao et al. (2019); Garcia-Gonzalez (2019); Mukherjee et al. (2021); Zhang et al. (2020); Garcia-Gonzalez and Hossain (2021a,b); Ye et al. (2021); Dadgar-Rad and Hossain (2022a); Moreno-Mateos et al. (2023); Liu et al. (2023); Stewart and Anand (2023)) or lattice- and micromechanics-based (e.g., Zhang et al. (2020); Garcia-Gonzalez and Hossain (2021a,b); Ye et al. (2021); Narayanan et al. (2023)) models have been developed to model deformation of HMSMs. In the continuum model developed by Zhao et al. (2019), instead of using the relation for the magnetic body couple, a novel energy term involving the internal magnetization vector and external magnetic flux has been added to the mechanical strain energy density. Their model has received considerable attention in recent years. In particular, various HMS beam formulations (Wang et al., 2020; Chen et al., 2021; Rajan and Arockiarajan, 2021; Yan et al., 2022;

Sano et al., 2022; Dadgar-Rad and Hossain, 2022b; Li et al., 2023) have been developed in the literature. Recently, an HMS plate formulation has been also developed by Yan et al. (2023). Dadgar-Rad and Hossain (2022a) noted that there are two drawbacks in the formulation of Zhao et al. (2019). The first drawback is that if the internal magnetic flux remains constant along a beam-like structure, the model just leads to two opposite concentrated forces at the two ends of the beam. Therefore, in this case, the model can predict only the deformation of cantilever beams made of HMSMs. The second drawback is that the model leads to normal stress and mechanical deformation if the internal and external magnetic fluxes are parallel to each other. Basically, in this case, the cross product of the two magnetic vectors is zero and no deformation must be observed in the structure. Due to the mentioned drawbacks, Dadgar-Rad and Hossain (2022a) developed the first micropolar-based formulation to model the deformation of HMSMs. The new formulation is based on calculating a body couple vector as a cross product of the internal and external magnetic fluxes. Therefore, neigher of the drawbacks observed in the formaltion of Zhao et al. (2019) occur in the micropolar-based model. The formulation was then extended to develop a micropolar shell model for HMSMS Dadgar-Rad and Hossain (2023).

A review of the literature reveals that there have been published a few papers dealing with the finite deformation of 3D beams based on micropolar theory. Moreover, away from the nature of formulation, the focus of researchers has been solving 2D examples. Accordingly, compared with the previous works, e.g. Obrezkov et al. (2022), the novelties of the present contribution are as follows:

- In contrast with the previous publications that mainly focus on the infinitesimal deformation of 2D beam problems, the present formulation starts by proposing a novel motion field that accounts for thickness change and can model large elastic deformation of 3D beams. Moreover, the undeformed beam may have arbitrary initial curvature.

- In the variational formulation of the present beam model, the effects of uniform and constant-gradient magnetic loading are taken into account. Therefore, beside capturing the size-effect phenomenon in purely mechanical problems, the formulation can also capture the finite deformation of HMS beams.

The rest of this paper is organized as follows: In Section 2, the basic kinematic quantities of the micropolar theory are presented. The kinematic equations describing the present micropolar beam model are introduced in Section 3. The variational formulation of the proposed beam model and the relations corresponding to the virtual internal energy and the virtual external work are provided in Section 4. A nonlinear finite element formulation in material framework is developed in Section 5. Several numerical examples are solved in Section 6 to demonstrate the applicability of the proposed formulation. Finally, the work is summarized in Section 7.

Notation: In this work, vectors and matrices are shown by the blackboard font, e.g., $\mathbb{X}$ and $\mathbb{K}$. Second-order tensors are shown by the boldface font, e.g., $\mathbf{F}$. Boldface calligraphic font is used for third-order and and fourth-order

tensor are disp, e.g., $\boldsymbol{\mathcal{E}}$ and $\boldsymbol{\mathcal{D}}$. Scalar quantities and the components of tensor quantities are not boldface and may be shown by Latin or Greek fonts, e.g, ψ and u_i. All Latin indices (both lower-case and upper-case) take values one, two and three, while Greek indices run over one and two. The summation convention holds over all repeated Latin and Greek indices. However, upper-case Latin indices with calligraphic font, e.g., $\{\mathcal{I}, \mathcal{J}, \mathcal{K}\}$, take the values specified in the corresponding equations. As usual, the notations $\mathbf{A}^{\mathsf{T}}$, $\mathrm{tr}\,\mathbf{A}$, $\det \mathbf{A}$ and $\mathbf{A}^{-1}$ are the transpose, trace, determinant and inverse of the second-order tensor $\mathbf{A}$. For the two arbitrary second-order tensors $\mathbf{A}$ and $\mathbf{B}$, the tensor products denoted by the symbols $\otimes$, $\odot$, and $\boxtimes$ are defined so that the relations $(\mathbf{A}\otimes\mathbf{B})_{ijkl} = A_{ij}B_{kl}$, $(\mathbf{A}\odot\mathbf{B})_{ijkl} = A_{ik}B_{jl}$, and $(\mathbf{A}\boxtimes\mathbf{B})_{ijkl} = A_{il}B_{kj}$ hold.

2. The basic kinematic quantities of the micropolar theory

The mathematical foundations of micropolar continuum theory have been developed by Eringen and his coworkers, e.g., Kafadar and Eringen (1971); Eringen and Kafadar (1976); Eringen (1999). In this section, some kinematic quantities of the theory, essential for the next developments, are introduced.

To start the formulation, two coincident Cartesian coordinate systems $\{X_1, X_2, X_3\}$ and $\{x_1, x_2, x_3\}$ with an arbitrary origin in the 3-space are considered. The orthonormal basis vectors corresponding to the introduced coordinate systems are denoted by $\{\mathbb{e}_1, \mathbb{e}_2, \mathbb{e}_3\}$ and $\{\mathbb{E}_1, \mathbb{E}_2, \mathbb{E}_3\}$, respectively. Moreover, the material and spatial gradient operators are defined by $\mathrm{Grad}\,\{\bullet\} = \frac{\partial\{\bullet\}}{\partial X_I}\otimes\mathbb{E}_I$ and $\mathrm{grad}\,\{\bullet\} = \frac{\partial\{\bullet\}}{\partial x_i}\otimes\mathbb{e}_i$, receptively.

As usual, the reference and current configurations of the continuum body at the times $t = 0$ and $t > 0$ are denoted by $\mathcal{B}_0$ and $\mathcal{B}$, respectively. The position vector $\mathbb{X} = X_I\mathbb{E}_I$ is defined as the center of a macro-element in $\mathcal{B}_0$. Deformation of the macro-element is governed by the mapping $\mathbb{x} = x_i\mathbb{e}_i = \mathbb{y}(\mathbb{X}, t)$, from which the macro displacement field $\bar{\mathbb{u}} = \mathbb{x} - \mathbb{X}$ is obtained. In the micropolar theory, it is assumed that there exists a micro-structure inside each macro-element that undergoes rigid micro-rotations. The micro-rotation of the micro-structure is described by the pseudo-vector field $\mathbb{q}$, and is independent from the macro-deformation field $\mathbb{y}$. The deformation gradient tensor $\mathbf{F}$, and the micro-rotation tensor $\tilde{\mathbf{R}}$ are given by

$$\mathbf{F} = \mathrm{Grad}\,\mathbb{y} = \mathbf{I} + \mathrm{Grad}\,\bar{\mathbb{u}}, \quad \tilde{\mathbf{R}} = \cos q\mathbf{I} - \sin q\boldsymbol{\mathcal{E}}\hat{\mathbb{q}} + (1-\cos q)\hat{\mathbb{q}}\otimes\hat{\mathbb{q}}, \tag{1}$$

where $\mathbf{I}$ is the identity tensor and $\boldsymbol{\mathcal{E}}$ is the alternating symbol. Moreover, $q = \sqrt{\mathbb{q}\cdot\mathbb{q}}$ is the magnitude of $\mathbb{q}$, and $\hat{\mathbb{q}} = \mathbb{q}/q$ is the unit vector along $\mathbb{q}$. Next, let $\delta\bar{\mathbb{u}}$ and $\delta\mathbb{q}$ be the virtual displacement and the virtual micro-rotation, respectively. Accordingly, straightforward calculations furnish the following expressions for $\delta\mathbf{F}$ and $\delta\tilde{\mathbf{R}}$:

$$\delta\mathbf{F} = \mathrm{Grad}\,\delta\mathbb{u}^{\star}, \quad \delta\tilde{\mathbf{R}} = \delta\tilde{\mathbf{Q}}\tilde{\mathbf{R}} = -\boldsymbol{\mathcal{E}}\delta\tilde{\mathbb{q}}\tilde{\mathbf{R}} \quad \text{with} \quad \delta\tilde{\mathbb{q}} = \boldsymbol{\Upsilon}\delta\mathbb{q}. \tag{2}$$

It is noted that $\delta\tilde{\mathbf{Q}} = -\boldsymbol{\mathcal{E}}\delta\tilde{\mathbb{q}}$ is the skew-symmetric tensor corresponding to $\delta\tilde{\mathbb{q}}$. Moreover, the second-order tensor $\boldsymbol{\Upsilon}$ is calculated to be

$$\boldsymbol{\Upsilon} = \frac{1}{q}[\sin q\mathbf{I} - (1-\cos q)\boldsymbol{\mathcal{E}}\hat{\mathbb{q}} + (q-\sin q)\hat{\mathbb{q}}\otimes\hat{\mathbb{q}}]. \tag{3}$$

In the material description of the micropolar theory, the second-order deformation measures $\tilde{\mathbf{U}}$ and $\boldsymbol{\Gamma}$ are defined as follows (e.g., Eringen and Kafadar (1976); Pietraszkiewicz and Eremeyev (2009); Steinmann (1994)):

$$\tilde{\mathbf{U}} = \tilde{\mathbf{R}}^{\top}\mathbf{F}, \quad \boldsymbol{\Gamma} = -\frac{1}{2}\boldsymbol{\mathcal{E}}:(\tilde{\mathbf{R}}^{\top}\mathrm{Grad}\,\tilde{\mathbf{R}}), \quad \tilde{U}_{MN} = \tilde{R}_{pM}F_{pN}, \quad \Gamma_{MN} = -\frac{1}{2}\epsilon_{MPQ}\tilde{R}_{pP}\tilde{R}_{pQ,N}, \tag{4}$$

where ϵ_{MPQ} are the components of the alternating symbol $\boldsymbol{\mathcal{E}}$. Moreover, since $\tilde{\mathbf{R}}$ is a rotation tensor, the relations $\det\tilde{\mathbf{R}} = 1$ and $\det\tilde{\mathbf{U}} = \det\mathbf{F} = J$ are deduced. From Eqs. (1), (2), and (4), it follows that the virtual micropolar deformation measures are given by

$$\delta\tilde{\mathbf{U}} = \tilde{\mathbf{R}}^{\top}(\delta\mathbf{F} - \delta\tilde{\mathbf{Q}}\mathbf{F}) = \tilde{\mathbf{R}}^{\top}(\delta\mathbf{F} + \boldsymbol{\mathcal{E}}\boldsymbol{\Upsilon}\delta\mathbb{q}\mathbf{F}), \quad \delta\boldsymbol{\Gamma} = \tilde{\mathbf{R}}^{\top}\mathrm{Grad}\,(\boldsymbol{\Upsilon}\delta\mathbb{q}). \tag{5}$$

In the next section, specialized forms of the micropolar deformation measures $\tilde{\mathbf{U}}$ and $\boldsymbol{\Gamma}$ for the proposed beam model are presented.

3. Kinematics of the 3D micropolar beam model

The geometry of a 3D beam in the reference and current configurations is illustrated in Fig. 1. The centreline of the beam in the reference configuration is denoted by $\mathcal{C}$, which deforms into the curve $\bar{\mathcal{C}}$ in the current one. In this work, the curve $\mathcal{C}$ is parametrized by the *arc-length* S. Now, let $\bar{\mathbb{X}}(S)$ be the position vector of material points on $\mathcal{C}$. Accordingly, the unit tangent vector $\mathbb{T} = T_I\mathbb{E}_I$, the unit principal normal vector $\mathbb{N} = N_I\mathbb{E}_I$, and the unit binormal vector $\mathbb{B} = B_I\mathbb{E}_I$ are given by (e.g., Sahraee and Wriggers (2023))

$$\mathbb{T}(S) = \bar{\mathbb{X}}'(S), \quad \mathbb{N}(S) = \frac{\mathbb{T}'(S)}{|\mathbb{T}'(S)|}, \quad \mathbb{B}(S) = \mathbb{T}(S)\times\mathbb{N}(S), \tag{6}$$

where $\{\bullet\}' = \partial\{\bullet\}/\partial S$ is the partial derivative w.r.t. the arc-length S. The triad of unit vectors $\{\mathbb{T},\mathbb{N},\mathbb{B}\}$ constitutes the Frenet frame on $\mathcal{C}$. Moreover, they may be considered as the *reference directors* in the present beam formulation. By differentiating the triad, the following well-known Frenet formulae are obtained (Sahraee and Wriggers, 2023):

$$\mathbb{T}' = \kappa\mathbb{N}, \quad \mathbb{N}' = -\kappa\mathbb{T} + \tau\mathbb{B}, \quad \mathbb{B}' = -\tau\mathbb{N}, \tag{7}$$

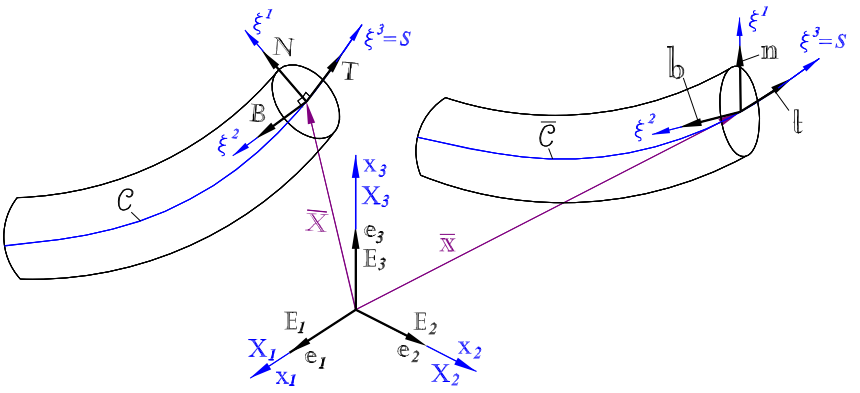

Figure 1: Schematic view of a 3D beam in reference (left) and current (right) configurations, $\{X_1, X_2, X_3\}$ and $\{x_1, x_2, x_3\}$ are the Cartesian coordinate systems, the Frenet triad $\{\mathbb{N}, \mathbb{B}, \mathbb{T}\}$ are tangent to the convective coordinate system $\{\xi^1, \xi^2, \xi^3\}$ in the reference configuration, the triad $\{\mathfrak{n}, \mathfrak{b}, \mathfrak{t}\}$ are tangent to $\{\xi^1, \xi^2, \xi^3\}$ in the current configuration

where $\kappa(S)$ and $\tau(S)$ are, respectively, the curvature and torsion of $\mathcal{C}$.

Next, as displayed in Fig. 1, the convective coordinate system $\{\xi^1, \xi^2, \xi^3 = S\}$ at each material point on the reference centreline $\mathcal{C}$ is considered. It is emphasized that the coordinated line ξ^3 is identical to the arc-length S and is always tangent to both $\mathcal{C}$ and $\bar{\mathcal{C}}$. Moreover, on the referential centreline $\mathcal{C}$, the coordinated lines ξ^1 and ξ^2 are in the directions of the vectors $\mathbb{N}$ and $\mathbb{B}$, respectively. It is worthwhile to note that the coordinate lines ξ^α do not necessarily remain perpendicular to $\bar{\mathcal{C}}$ in the current configuration. Now, the position vector of any material particle of the undeformed beam may be described by

$$\mathbb{X}(\xi^1, \xi^2, S) = \bar{\mathbb{X}}(S) + \xi^1 \mathbb{N}(S) + \xi^2 \mathbb{B}(S). \tag{8}$$

From Eqs. (7) and (8), the covariant basis vectors $\mathbb{G}_i(\xi^1, \xi^2, S) = \partial \mathbb{X} / \partial \xi^i$ and the contravariant ones $\mathbb{G}^i(\xi^1, \xi^2, S) = \partial \xi^i / \partial \mathbb{X}$ are calculated to be

$$\left.\begin{aligned} &\mathbb{G}_1 = \mathbb{N}, \quad \mathbb{G}_2 = \mathbb{B}, \quad \mathbb{G}_3 = (1 - \xi^1 \kappa)\mathbb{T} + \tau(\xi^1 \mathbb{B} - \xi^2 \mathbb{N}) \\ &\mathbb{G}^1 \approx \mathbb{N} + \xi^2 \tau_0 \mathbb{T}, \quad \mathbb{G}^2 \approx \mathbb{B} - \xi^1 \tau_0 \mathbb{T}, \quad \mathbb{G}^3 \approx (1 + \xi^1 \kappa)\mathbb{T} \end{aligned}\right\}. \tag{9}$$

It is noted that the relation $\mathbb{G}_i \cdot \mathbb{G}^j = \delta_i^j$ holds.

In the sequel, a finite deformation Timoshenko-type beam model is developed. The model may be considered as the beam version of the shell formulation elaborated by (Sansour, 1998). To do so, let $\mathbb{w}(S, t) = w_i \mathbb{e}_i$ be the displacement field of the centreline, which takes the referential position $\bar{\mathbb{X}}$ to the current one $\bar{\mathbb{x}} = \bar{\mathbb{X}} + \mathbb{w}$. Additionally, let the vectors $\mathbb{u}(S, t) = u_i \mathbb{e}_i$ and $\mathbb{v}(S, t) = v_i \mathbb{e}_i$ be the director displacements from which the current directors $\mathfrak{n} = \mathbb{N} + \mathbb{u}$ and $\mathfrak{b} = \mathbb{B} + \mathbb{v}$ are obtained. Furthermore, the scalar functions $\phi(S, t)$ and $\psi(S, t)$ are introduced to account for

the thickness change in the ξ^1 and ξ^2 directions, respectively. Accordingly, the following motion field for the macro-deformation of the present beam model is introduced:

$$\mathbb{x} = \mathbb{y}(\xi^1, \xi^2, S) = \bar{\mathbb{x}}(S) + \xi^1[1 + \xi^1\phi(S)]\mathbb{n}(S) + \xi^2[1 + \xi^2\psi(S)]\mathbb{b}(S). \tag{10}$$

It is noted that by introducing the thickness stretching parameters $\phi(S,t)$ and $\psi(S,t)$, the normal strains and normal stresses along the ξ^1 and ξ^2 coordinates will be nonzero. This allows one to use three-dimensional constitutive equations without any modification to satisfy the plane stress conditions $\sigma_{11} = \sigma_{22} = 0$ along the ξ^1 and ξ^2 directions. Since the vector $\mathbb{t} = \bar{\mathbb{x}}' = \mathbb{T} + \mathbb{w}'$ is tangent to the deformed centreline $\bar{\mathcal{C}}$, it is concluded that the triad $\{\mathbb{t}, \mathbb{n}, \mathbb{b}\}$ forms the *current directors* of the beam.

Now, with Eqs. (7) and (10), the current covariant basis vectors $\mathbb{g}_i(\xi^1, \xi^2, S) = \partial\mathbb{x}/\partial\xi^i$ are obtained to be

$$\mathbb{g}_1 = (1 + 2\xi^1\phi)\mathbb{n}, \quad \mathbb{g}_2 = (1 + 2\xi^2\psi)\mathbb{b}, \quad \mathbb{g}_3 = \mathbb{t} + \xi^1(\tau\mathbb{B} - \kappa\mathbb{T} + \mathbb{u}') + \xi^2(\mathbb{v}' - \tau\mathbb{N}). \tag{11}$$

From Eqs. (9) and (11), it follows that the deformation gradient tensor is given by

$$\mathbf{F} = \mathbb{g}_i \otimes \mathbb{G}^i \approx \mathbf{F}_0 + \xi^\alpha \mathbf{F}_\alpha, \tag{12}$$

where the higher-order terms involving $\xi^\alpha\xi^\beta$ are neglected. Moreover, the tensors $\mathbf{F}_\mathcal{I}$ ($\mathcal{I} = 0, 1, 2$) are calculated to be

$$\left.\begin{aligned} \mathbf{F}_0 &= \mathbf{I} + \mathbb{u} \otimes \mathbb{N} + \mathbb{v} \otimes \mathbb{B} + \mathbb{w}' \otimes \mathbb{T} \\ \mathbf{F}_1 &= 2\phi\mathbb{n} \otimes \mathbb{N} + (\kappa\mathbb{w}' - \tau\mathbb{v} + \mathbb{u}') \otimes \mathbb{T} \\ \mathbf{F}_2 &= 2\psi\mathbb{b} \otimes \mathbb{B} + (\mathbb{v}' + \tau\mathbb{u}) \otimes \mathbb{T} \end{aligned}\right\}. \tag{13}$$

Next, following Ramezani et al. (2009a) it is assumed that the micro-rotation $\mathbb{q}$ is constant at each cross-section of the beam. Now, from Eqs. (4), (9), and (12), the micropolar deformation tensors $\tilde{\mathbf{U}}$ and $\boldsymbol{\Gamma}$ for the present beam model take the following forms:

$$\tilde{\mathbf{U}} = \tilde{\mathbf{U}}_0 + \xi^\alpha\tilde{\mathbf{U}}_\alpha, \quad \boldsymbol{\Gamma} = \boldsymbol{\Gamma}_0 + \xi^1\boldsymbol{\Gamma}_1, \tag{14}$$

where $\tilde{\mathbf{U}}_\mathcal{I}$ ($\mathcal{I} = 0, 1, 2$) and $\boldsymbol{\Gamma}_\mathcal{J}$ ($\mathcal{J} = 0, 1$) are calculated to be

$$\tilde{\mathbf{U}}_\mathcal{I} = \tilde{\mathbf{R}}^\mathsf{T}\mathbf{F}_\mathcal{I}, \quad \boldsymbol{\Gamma}_0 = -\frac{1}{2}\boldsymbol{\mathcal{E}} : \left[\tilde{\mathbf{R}}^\mathsf{T}(\tilde{\mathbf{R}}' \otimes \mathbb{T})\right], \quad \boldsymbol{\Gamma}_1 = \kappa\boldsymbol{\Gamma}_0. \tag{15}$$

For later use, from Eqs. (13) and $(14)_1$, the expressions for $J = \det \mathbf{F}$, $\ln J$, and $\tilde{\mathbf{U}}^{-\mathsf{T}}$ may be approximately written as

$$J \approx J_0 + \xi^\alpha J_\alpha, \quad \ln J \approx J_0^\star + \xi^\alpha J_\alpha^\star, \quad \tilde{\mathbf{U}}^{-\mathsf{T}} \approx \tilde{\mathbf{U}}_0^\star + \xi^\alpha \tilde{\mathbf{U}}_\alpha^\star, \tag{16}$$

where $J_{\mathcal{I}}$, $J_{\mathcal{I}}^\star$, and $\tilde{\mathbf{U}}_{\mathcal{I}}^\star$ ($\mathcal{I} = 0, 1, 2$) are as follows:

$$J_0 = \det \mathbf{F}_0, \quad J_\alpha = J_0 \mathrm{tr}(\mathbf{F}_0^{-1}\mathbf{F}_\alpha), \quad J_0^\star = \ln J_0, \quad J_\alpha^\star = J_\alpha / J_0, \quad \tilde{\mathbf{U}}_0^\star = \tilde{\mathbf{U}}_0^{-\mathsf{T}}, \quad \tilde{\mathbf{U}}_\alpha^\star = -\tilde{\mathbf{U}}_0^\star \tilde{\mathbf{U}}_\alpha^{\mathsf{T}} \tilde{\mathbf{U}}_0^\star. \tag{17}$$

4. Variational formulation of the beam model

The purpose of this section is to develop the expressions for the virtual internal energy $\delta\mathcal{U}$ and the virtual work of external loads $\delta\mathcal{W}$ for the present micropolar beam model. In the next section, these quantities are used in the principle of virtual work of the form $\delta\mathcal{U} - \delta\mathcal{W} = 0$ to develop a finite element formulation.

4.1. Virtual internal energy

To develop the expression for the virtual internal energy $\delta\mathcal{U}$ in the material framework, the strain energy per unit reference volume must be of the form $\hat{\mathcal{U}} = \bar{\mathcal{U}}(\tilde{\mathbf{U}}, \boldsymbol{\Gamma})$ (Eringen and Kafadar, 1976; Steinmann, 1994; Ramezani et al., 2009b), from which it follows that

$$\delta\hat{\mathcal{U}} = \delta\bar{\mathcal{U}}(\tilde{\mathbf{U}}, \boldsymbol{\Gamma}) = \tilde{\mathbf{P}} : \delta\tilde{\mathbf{U}} + \tilde{\mathbf{M}} : \delta\boldsymbol{\Gamma} \quad \text{with} \quad \tilde{\mathbf{P}} = \frac{\partial\bar{\mathcal{U}}}{\partial\tilde{\mathbf{U}}} \quad \text{and} \quad \tilde{\mathbf{M}} = \frac{\partial\bar{\mathcal{U}}}{\partial\boldsymbol{\Gamma}}. \tag{18}$$

It is noted that $\tilde{\mathbf{P}}$ and $\tilde{\mathbf{M}}$ are the *material* or *Lagrangian* stress and couple stress tensors, respectively. In the micropolar theory, it is also possible to define the first Piola–Kirchhoff-type stress $\mathbf{P} = \tilde{\mathbf{R}}\tilde{\mathbf{P}}$ and couple stress $\mathbf{M} = \tilde{\mathbf{R}}\tilde{\mathbf{M}}$ tensors (e.g., Dadgar-Rad and Hossain (2022a)). As a special case of the strain energy density function $\bar{\mathcal{U}}(\tilde{\mathbf{U}}, \boldsymbol{\Gamma})$, a micropolar extension of the neo-Hookean material model may be written as

$$\bar{\mathcal{U}}(\tilde{\mathbf{U}}, \boldsymbol{\Gamma}) = \bar{\mathcal{U}}_1(\tilde{\mathbf{U}}) + \bar{\mathcal{U}}_2(J) + \bar{\mathcal{U}}_3(\boldsymbol{\Gamma}), \tag{19}$$

where $\bar{\mathcal{U}}_{\mathcal{I}}$ ($\mathcal{I} = 1, 2, 3$) are given by (Ramezani et al., 2009b; Dadgar-Rad and Hossain, 2022a)

$$\bar{\mathcal{U}}_1(\tilde{\mathbf{U}}) = (\eta + \tfrac{1}{2}\mu)\mathrm{tr}(\tilde{\mathbf{U}}\tilde{\mathbf{U}}^{\mathsf{T}}) - \eta\mathrm{tr}(\tilde{\mathbf{U}}^2), \quad \bar{\mathcal{U}}_2(J) = \frac{1}{2}\lambda(\ln J)^2 - \mu \ln J, \quad \bar{\mathcal{U}}_3(\boldsymbol{\Gamma}) = \frac{1}{2}\beta\mathrm{tr}(\boldsymbol{\Gamma}\boldsymbol{\Gamma}^{\mathsf{T}}). \tag{20}$$

Here, λ and μ are the usual Lamé constants. However, the constant η and β are two additional material parameters of the micropolar theory. In particular, the parameter β is often written in the form $\beta = \mu l^2$, where l is called the material

length-scale parameter, e.g., Steinmann (1994) and Bauer et al. (2012a). From Eqs. (14), (16), $(18)_{2,3}$, (19), and (20), the following expressions for the stress and couple stress measures $\tilde{\mathbf{P}}$, $\tilde{\mathbf{M}}$, $\mathbf{P}$, and $\mathbf{M}$ are obtained:

$$\tilde{\mathbf{P}} = \tilde{\mathbf{P}}_0 + \xi^\alpha \tilde{\mathbf{P}}_\alpha, \quad \mathbf{P} = \mathbf{P}_0 + \xi^\alpha \mathbf{P}_\alpha, \quad \tilde{\mathbf{M}} = \tilde{\mathbf{M}}_0 + \xi^1 \tilde{\mathbf{M}}_1, \quad \mathbf{M} = \mathbf{M}_0 + \xi^1 \mathbf{M}_1, \tag{21}$$

where the second-order tensors $\tilde{\mathbf{P}}_\mathcal{I}$, $\tilde{\mathbf{P}}_\mathcal{I}$, $\tilde{\mathbf{M}}_\mathcal{J}$, and $\mathbf{M}_\mathcal{J}$ (with $\mathcal{I} = 0, 1, 2$ and $\mathcal{J} = 0, 1$) are calculated to be

$$\left.\begin{aligned} \tilde{\mathbf{P}}_0 &= \mu \tilde{\mathbf{U}}_0 + \eta(\tilde{\mathbf{U}}_0 - \tilde{\mathbf{U}}_0^\top) + (\lambda J_0^\star - \mu)\tilde{\mathbf{U}}_0^\star \\ \tilde{\mathbf{P}}_\alpha &= \mu \tilde{\mathbf{U}}_\alpha + \eta(\tilde{\mathbf{U}}_\alpha - \tilde{\mathbf{U}}_\alpha^\top) + (\lambda J_0^\star - \mu)\tilde{\mathbf{U}}_\alpha^\star + \lambda J_\alpha^\star \tilde{\mathbf{U}}_0^\star \\ \tilde{\mathbf{M}}_\mathcal{J} &= \mu l^2 \boldsymbol{\Gamma}_\mathcal{J}, \quad \mathbf{P}_\mathcal{I} = \tilde{\mathbf{R}}\tilde{\mathbf{P}}_\mathcal{I}, \quad \mathbf{M}_\mathcal{J} = \tilde{\mathbf{R}}\tilde{\mathbf{M}}_\mathcal{J} \end{aligned}\right\}. \tag{22}$$

Moreover, the fourth-order tensors $\tilde{\boldsymbol{\mathcal{D}}}^\mathcal{I}$ ($\mathcal{I} = 1, 2$) resulting from the present constitutive model are given by

$$\tilde{\boldsymbol{\mathcal{D}}}^1 = \frac{\partial^2 \bar{\mathcal{U}}}{\partial \tilde{\mathbf{U}} \partial \tilde{\mathbf{U}}} \approx \tilde{\boldsymbol{\mathcal{D}}}_0^1 + \xi^\alpha \tilde{\boldsymbol{\mathcal{D}}}_\alpha^1, \quad \tilde{\boldsymbol{\mathcal{D}}}^2 = \frac{\partial^2 \bar{\mathcal{U}}}{\partial \boldsymbol{\Gamma} \partial \boldsymbol{\Gamma}} = \mu l^2 \mathbf{I} \odot \mathbf{I}, \tag{23}$$

where the fourth-order tensors $\tilde{\boldsymbol{\mathcal{D}}}_\mathcal{I}^1$ ($\mathcal{I} = 0, 1, 2$) are as follows:

$$\left.\begin{aligned} \tilde{\boldsymbol{\mathcal{D}}}_1^1 &= (\mu + \eta)\mathbf{I} \odot \mathbf{I} - \eta \mathbf{I} \boxtimes \mathbf{I} + \lambda \tilde{\mathbf{U}}_0^\star \otimes \tilde{\mathbf{U}}_0^\star + (\mu - \lambda J_0^\star)\tilde{\mathbf{U}}_0^\star \boxtimes \tilde{\mathbf{U}}_0^\star \\ \tilde{\boldsymbol{\mathcal{D}}}_\alpha^1 &= \lambda(\tilde{\mathbf{U}}_0^\star \otimes \tilde{\mathbf{U}}_\alpha^\star + \tilde{\mathbf{U}}_\alpha^\star \otimes \tilde{\mathbf{U}}_0^\star - J_\alpha^\star \tilde{\mathbf{U}}_0^\star \boxtimes \tilde{\mathbf{U}}_0^\star) + (\mu - \lambda J_0^\star)(\tilde{\mathbf{U}}_0^\star \boxtimes \tilde{\mathbf{U}}_\alpha^\star + \tilde{\mathbf{U}}_\alpha^\star \boxtimes \tilde{\mathbf{U}}_0^\star) \end{aligned}\right\}. \tag{24}$$

In the next step, from Eqs. (5) and $(18)_1$, the virtual internal energy $\delta\mathcal{U}$ may be written as

$$\delta\mathcal{U} = \int_\mathcal{V} \delta\hat{\mathcal{U}} \mathrm{d}\mathcal{V} = \int_\mathcal{V} (\mathbf{P} : \delta\mathbf{Y} + \mathbf{M} : \delta\mathbf{Z}) \mathrm{d}\mathcal{V} \quad \text{with} \quad \delta\mathbf{Y} = \delta\mathbf{Y}_0 + \xi^\alpha \delta\mathbf{Y}_\alpha \quad \text{and} \quad \delta\mathbf{Z} = (1 + \xi^1\kappa)\delta\mathbf{Y}_3. \tag{25}$$

Here, $\mathcal{V}$ is the reference volume of the beam, and the quantities denoted by $\delta\mathbf{Y}_\mathcal{I}$ ($\mathcal{I} = 0, 1, 2, 3$) are defined by

$$\delta\mathbf{Y}_\mathcal{J} = \delta\mathbf{F}_\mathcal{J} - \delta\tilde{\mathbf{Q}}\mathbf{F}_\mathcal{J}, \quad \delta\mathbf{Y}_3 = (\mathbf{Y}\delta\mathfrak{q})' \otimes \mathbb{T}, \quad (\mathcal{J} = 0, 1, 2). \tag{26}$$

The volume element may be written as $\mathrm{d}\mathcal{V} = \mathrm{d}\mathcal{A}\mathrm{d}S$, where $\mathrm{d}\mathcal{A}$ is an infinitesimal area element. Consequently, the expression for $\delta\mathcal{U}$ reduces to the following line integral along the referential centreline C of the beam:

$$\delta\mathcal{U} = \int_C \left(\mathcal{A}\mathbf{P}_0 : \delta\mathbf{Y}_0 + \mathcal{I}_{\alpha\beta}\mathbf{P}_\alpha : \delta\mathbf{Y}_\beta + \mathcal{I}_{11}^\star \mathbf{M}_0 : \delta\mathbf{Y}_3\right) \mathrm{d}S, \tag{27}$$

where $\mathcal{I}_{\alpha\beta}$ and $\mathcal{I}^{\star}_{11}$ are defined as

$$\mathcal{I}_{\alpha\beta}(S) = \int_{\mathcal{A}(S)} \xi^{\alpha}\xi^{\beta}\mathrm{d}\mathcal{A}, \quad \mathcal{I}^{\star}_{11}(S) = \mathcal{A}(S) + \kappa^2(S)\mathcal{I}_{11}(S). \tag{28}$$

It is noted that $\mathcal{I}_{\alpha\beta}$ are the cross-sectional moments of inertia. In the next step, the fourth-order tensors $\boldsymbol{\mathcal{D}}^{\mathcal{I}}$ $(\mathcal{I} = 1, 2)$ are defined so that their components are given by $\mathcal{D}^{\mathcal{I}}_{iJkL} = \tilde{R}_{iP}\tilde{R}_{kQ}\tilde{\mathcal{D}}^{\mathcal{I}}_{PJQL}$. From this definition and Eq. $(23)_1$, the relation $\mathcal{D}^{1}_{\mathcal{K}iJkL} = \tilde{R}_{iP}\tilde{R}_{kQ}\tilde{\mathcal{D}}^{1}_{\mathcal{K}PJQL}$ $(\mathcal{K} = 0, 1, 2)$ is also deduced. Accordingly, from Eqs. (18) and (25), the increment of the virtual internal energy, $\Delta\delta\mathcal{U}$, is calculated as follows:

$$\Delta\delta\mathcal{U} = \int_{\mathcal{V}} \big[\delta\mathbf{Y}:\boldsymbol{\mathcal{D}}^{1}:\Delta\mathbf{Y} + \delta\mathbf{Z}:\boldsymbol{\mathcal{D}}^{2}:\Delta\mathbf{Z} + \mathbf{P}:(\Delta\delta\mathbf{H}_0 + \xi^{\alpha}\Delta\delta\mathbf{H}_{\alpha}) + (1+\kappa\xi^{1})\mathbf{M}:\Delta\delta\mathbf{H}_3\big]\mathrm{d}\mathcal{V}. \tag{29}$$

Here, the quantities denoted by $\Delta\delta\mathbf{H}_{\mathcal{J}}$ $(\mathcal{J} = 0, 1, 2, 3)$ are defined as follows:

$$\left.\begin{aligned} \Delta\delta\mathbf{H}_{\mathcal{I}} &= (\Delta\tilde{\mathbf{Q}}\delta\tilde{\mathbf{Q}} - \Delta\delta\tilde{\mathbf{Q}})\mathbf{F}_{\mathcal{I}} - \delta\tilde{\mathbf{Q}}\Delta\mathbf{F}_{\mathcal{I}} - \Delta\tilde{\mathbf{Q}}\delta\mathbf{F}_{\mathcal{I}} \\ \Delta\delta\mathbf{H}_3 &= [(\Delta\boldsymbol{\Upsilon}\delta\mathbb{q})' - \Delta\tilde{\mathbf{Q}}(\boldsymbol{\Upsilon}\delta\mathbb{q})'] \otimes \mathbb{T} \end{aligned}\right\}, \quad \mathcal{I} = 0, 1, 2. \tag{30}$$

With Eqs. (21), (23), (25), and (29), the expressions for the increment of virtual internal energy may be written as $\Delta\delta\mathcal{U} = \Delta\delta\mathcal{U}_1 + \Delta\delta\mathcal{U}_2$, with:

$$\left.\begin{aligned} \Delta\delta\mathcal{U}_1 &= \int_{\mathcal{C}} \big[\mathcal{I}_{\alpha\beta}(\delta\mathbf{Y}_0:\boldsymbol{\mathcal{D}}^{1}_{\alpha}:\Delta\mathbf{Y}_{\beta} + \delta\mathbf{Y}_{\alpha}:\boldsymbol{\mathcal{D}}^{1}_{0}:\Delta\mathbf{Y}_{\beta} + \delta\mathbf{Y}_{\alpha}:\boldsymbol{\mathcal{D}}^{1}_{\beta}:\Delta\mathbf{Y}_0) \\ &\qquad + \mathcal{A}\delta\mathbf{Y}_0:\boldsymbol{\mathcal{D}}^{1}_{0}:\Delta\mathbf{Y}_0 + \mathcal{I}^{\star}_{11}\delta\mathbf{Y}_3:\boldsymbol{\mathcal{D}}^{2}:\Delta\mathbf{Y}_3\big]\mathrm{d}S \\ \Delta\delta\mathcal{U}_2 &= \int_{\mathcal{C}} \big(\mathcal{I}_{\alpha\beta}\mathbf{P}_{\alpha}:\Delta\delta\mathbf{H}_{\beta} + \mathcal{A}\mathbf{P}_0:\Delta\delta\mathbf{H}_0 + \mathcal{I}^{\star}_{11}\mathbf{M}_0:\Delta\delta\mathbf{H}_3\big)\mathrm{d}S \end{aligned}\right\}. \tag{31}$$

4.2. Virtual external work due to magnetic loading

In this section, it is assumed that the beam has been made of HMSMs, and exhibits finite mechanical deformations under magnetic loading. It is recalled that there exists a strong remnant magnetic flux density in HMSMs, which remains almost unchanged under a wide range of external magnetic loading. In this work, the influence of the self-applied magnetic field produced by the presence and movement of the hard magnetic particles is neglected. Under the external magnetic flux $\mathbb{B}^{\mathrm{ext}}$, the body couple per unit reference volume $\mathbb{m}$ applied to HMSMs is given by (Zhao et al., 2019)

$$\mathbb{m} = \frac{1}{\mu_0}\boldsymbol{J}\mathbb{B}^{\mathrm{rem}} \times \mathbb{B}^{\mathrm{ext}} = \frac{1}{\mu_0}\big(\mathbf{F}\tilde{\mathbb{B}}^{\mathrm{rem}}\big) \times \mathbb{B}^{\mathrm{ext}} \quad \text{with} \qquad \mathbb{B}^{\mathrm{rem}} = \boldsymbol{J}^{-1}\mathbf{F}\tilde{\mathbb{B}}^{\mathrm{rem}}. \tag{32}$$

Here, $\tilde{\mathbb{B}}^{\text{rem}}$ and $\mathbb{B}^{\text{rem}}$ are the remnant magnetic flux densities in the reference and current configurations, respectively. Moreover, $\mu_0 = 4\pi \times 10^{-7}\,\frac{N}{A^2}$ is the magnetic permeability of the free space. It is noted that both $\mathbb{B}^{\text{rem}}$ and $\mathbb{B}^{\text{ext}}$ are Eulerian (or spatial) vectors. However $\mathbb{m}$ is the body couple per unit *reference* volume of the continuum body.

Remark. Based upon computational homogenization on HMSMs, Mukherjee et al. (2021) showed that the right stretch tensor $\mathbf{U}$ does not have a significant role in the mapping of the referential remnant magnetic flux $\tilde{\mathbb{B}}^{\text{rem}}$ to the current one $\mathbb{B}^{\text{rem}}$. Accordingly, they have proposed to replace Eq. $(32)_2$ with $\mathbb{B}^{\text{rem}} = \mathbf{R}\tilde{\mathbb{B}}^{\text{rem}}$. Here, $\mathbf{R}$ is the rotation tensor in the polar decomposition $\mathbf{F} = \mathbf{R}\mathbf{U}$. On the other hand, if the amount of strain in a deformation is small, namely $\mathbf{U} \approx \mathbf{I}$, the deformation gradient is approximately equal to the rotation tensor, giving $\mathbf{F} \approx \mathbf{R}$. More precisely, a limitation of the present formulation is that it works well for the cases where the amount of strain is small. Accordingly, in Section 6, four examples with bending-dominated deformations are studied.

If the external magnetic flux $\mathbb{B}^{\text{ext}}$ is non-uniform, its spatial gradient is nonzero. In this case, in addition to the body couple density $\mathbb{m}$, the following body force per unit reference volume $\mathbb{f}$ is also induced in HMSMs (Yan et al., 2022):

$$\mathbb{f} = \frac{1}{\mu_0} J\mathbf{G}^{\text{ext}}\mathbb{B}^{\text{rem}} = \frac{1}{\mu_0}\mathbf{G}^{\text{ext}}\mathbf{F}\tilde{\mathbb{B}}^{\text{rem}} \quad \text{with} \quad \mathbf{G}^{\text{ext}} = (\text{grad}\,\mathbb{B}^{\text{ext}})^{\mathsf{T}}. \tag{33}$$

As a practical example of non-uniform magnetic loading, in a Maxwell coil with an axis along the $\mathbb{e}_3$ direction, the magnetic field and its spatial gradient are given by (Yan et al., 2022; Sano et al., 2022)

$$\mathbb{B}^{\text{ext}} = -\frac{1}{2}b(r\mathbb{e}_r - 2x_3\mathbb{e}_3) = -\frac{1}{2}b(x_1\mathbb{e}_1 + x_2\mathbb{e}_2 - 2x_3\mathbb{e}_3), \quad \mathbf{G}^{\text{ext}} = -\frac{1}{2}\text{diag}[b, b, -2b], \tag{34}$$

where b is the intensity of the magnetic field per unit length, and $\mathbb{e}_r$ is the unit vector along the radial direction of the coil. In this case, the tensor $\mathbf{G}^{\text{ext}}$ is constant, and the field resulting from the coil is referred to as the *constant gradient field*. In the next developments, it is assumed that $\mathbf{G}^{\text{ext}}$ is constant. In particular, for the present beam model, from Eqs. (12) and (33) it follows that

$$\mathbb{f} = \frac{1}{\mu_0}(\mathbb{f}_0 + \xi^\alpha \mathbb{f}_\alpha) \quad \text{with} \quad \mathbb{f}_{\mathcal{I}} = \mathbf{G}^{\text{ext}}\mathbf{F}_{\mathcal{I}}\tilde{\mathbb{B}}^{\text{rem}} \quad (\mathcal{I} = 0, 1, 2). \tag{35}$$

In the next step, it is noted that the body force density $\mathbb{f}$ and the body couple density $\mathbb{m}$ are work-conjugate to the macro-displacement $\bar{\mathbb{u}}$ and the micro-rotation $\mathbb{q}$, respectively. With Eqs. (10), (32), (33), and (35), the virtual external

work may be written as follows:

$$\begin{aligned}\delta\mathcal{W} &= \int_{\mathcal{V}} (\mathbb{f}\cdot\delta\bar{\mathbb{u}} + \mathbb{m}\cdot\delta\mathbb{q})\mathrm{d}\mathcal{V} \\ &= \frac{1}{\mu_0}\int_C \big\{ I_{11}[(\delta\boldsymbol{\phi}\mathbb{m} + \boldsymbol{\phi}\delta\mathbb{u})^{\mathsf{T}}\mathbb{f}_0 + \delta\mathbb{u}^{\mathsf{T}}\mathbb{f}_1] + I_{22}[(\delta\boldsymbol{\psi}\mathbb{b} + \boldsymbol{\psi}\delta\mathbb{v})^{\mathsf{T}}\mathbb{f}_0 + \delta\mathbb{v}^{\mathsf{T}}\mathbb{f}_2] \\ &\qquad + I_{12}(\delta\mathbb{u}^{\mathsf{T}}\mathbb{f}_2 + \delta\mathbb{v}^{\mathsf{T}}\mathbb{f}_1) + \mathcal{A}(\delta\mathbb{w}^{\mathsf{T}}\mathbb{f}_0 + \mathbb{q}^{\mathsf{T}}[(\mathbf{F}_0\tilde{\mathbb{B}}^{\mathrm{rem}})\times\mathbb{B}^{\mathrm{ext}}])\big\}\mathrm{d}S.\end{aligned} \tag{36}$$

Moreover, the increment of $\delta\mathcal{W}$ takes the form

$$\begin{aligned}\Delta\delta\mathcal{W} = \frac{1}{\mu_0}\int_C \big\{ &\mathcal{I}_{11}[(\delta\boldsymbol{\phi}\mathbb{m} + \boldsymbol{\phi}\delta\mathbb{u})^{\mathsf{T}}\Delta\mathbb{f}_0 + \delta\mathbb{u}^{\mathsf{T}}\Delta\mathbb{f}_1 + \delta\boldsymbol{\phi}\mathbb{f}_0^{\mathsf{T}}\Delta\mathbb{u} + \delta\mathbb{u}^{\mathsf{T}}\mathbb{f}_0\Delta\boldsymbol{\phi}] \\ &+ \mathcal{I}_{22}[(\delta\boldsymbol{\psi}\mathbb{b} + \boldsymbol{\psi}\delta\mathbb{v})^{\mathsf{T}}\Delta\mathbb{f}_0 + \delta\mathbb{v}^{\mathsf{T}}\Delta\mathbb{f}_2 + \delta\boldsymbol{\psi}\mathbb{f}_0^{\mathsf{T}}\Delta\mathbb{v} + \delta\mathbb{v}^{\mathsf{T}}\mathbb{f}_0\Delta\boldsymbol{\psi}] \\ &+ \mathcal{I}_{12}(\delta\mathbb{u}^{\mathsf{T}}\Delta\mathbb{f}_2 + \delta\mathbb{v}^{\mathsf{T}}\Delta\mathbb{f}_1) + \mathcal{A}(\delta\mathbb{w}^{\mathsf{T}}\Delta\mathbb{f}_0 + \delta\mathbb{q}^{\mathsf{T}}[(\Delta\mathbf{F}_0\tilde{\mathbb{B}}^{\mathrm{rem}})\times\mathbb{B}^{\mathrm{ext}}])\big\}\mathrm{d}S,\end{aligned} \tag{37}$$

where $\Delta\mathbb{f}_{\mathcal{I}} = \mathbf{G}^{\mathrm{ext}}\Delta\mathbf{F}_{\mathcal{I}}\tilde{\mathbb{B}}^{\mathrm{rem}}$ ($\mathcal{I} = 0, 1, 2$) is deduced from Eqs. (12) and (35).

5. Nonlinear finite element formulation

In this section, a Total Lagrangian nonlinear finite element formulation for the numerical solution of problems based on the present model is developed. The centreline C is discretized into N_E elements, namely $C = \bigcup_{\mathrm{e}=1}^{N_E} C^{\mathrm{e}}$. The field variables $\{u_i, v_i, w_i, q_i, \phi, \psi\}$ over the typical element C^{e} are interpolated in the following form:

$$\{u_i, v_i, w_i, q_i, \phi, \psi\} = \{\mathbb{N}_{\mathsf{u}}\mathbb{U}_i, \mathbb{N}_{\mathsf{v}}\mathbb{V}_i, \mathbb{N}_{\mathsf{w}}\mathbb{W}_i, \mathbb{N}_{\mathsf{q}}\mathbb{Q}_i, \mathbb{N}_{\mathsf{h}}\boldsymbol{\Phi}, \mathbb{N}_{\mathsf{s}}\boldsymbol{\Psi}\}, \quad i = 1, 2, 3. \tag{38}$$

Here, as an example, the row vector $\mathbb{N}_{\mathsf{w}}$ and the corresponding column vector $\mathbb{W}_i$ are explained in detail. Let n_{w} be the number of nodes of the element that possess the w_i degrees of freedom (DOFs). Additionally, let $N_{\mathsf{w}}^{\mathcal{I}}$, with $\mathcal{I} = 1, 2, ..., n_{\mathsf{w}}$, be the shape functions that interpolate the displacement component w_i over the element. Furthermore, let $W_i^{\mathcal{I}}$ be the nodal value of w_i at the $\mathcal{I}$'th node of the element. Accordingly, $\mathbb{N}_{\mathsf{w}} = \{N_{\mathsf{w}}^1, N_{\mathsf{w}}^2, ..., N_{\mathsf{w}}^{n_{\mathsf{w}}}\}$ is a row vector that contains the shape functions $N_{\mathsf{w}}^{\mathcal{I}}$, and $\mathbb{W}_i = \{W_i^1, W_i^2, ..., W_i^{n_{\mathsf{w}}}\}^{\mathsf{T}}$ is a column vector that involves the nodal DOFs $W_i^{\mathcal{I}}$. The other quantities in Eq. (38) have similar definitions. It is worthwhile to note that the interpolation of the director displacements $\mathbb{u}$ and $\mathbb{v}$ in the present work is equivalent to the interpolation of the director vectors advocated in Betsch and Steinmann (2002). The generalized displacement vector $\mathbb{d}^{\mathrm{e}}$ that involves all nodal DOFs of the element is defined as follows:

$$\mathbb{d}^{\mathrm{e}}_{n_{\mathrm{e}}\times 1} = \{\mathbb{U}_1^{\mathsf{T}}, \mathbb{U}_2^{\mathsf{T}}, \mathbb{U}_3^{\mathsf{T}}, \mathbb{V}_1^{\mathsf{T}}, \mathbb{V}_2^{\mathsf{T}}, \mathbb{V}_3^{\mathsf{T}}, \mathbb{W}_1^{\mathsf{T}}, \mathbb{W}_2^{\mathsf{T}}, \mathbb{W}_3^{\mathsf{T}}, \mathbb{Q}_1^{\mathsf{T}}, \mathbb{Q}_2^{\mathsf{T}}, \mathbb{Q}_3^{\mathsf{T}}, \boldsymbol{\Phi}^{\mathsf{T}}, \boldsymbol{\Psi}^{\mathsf{T}}\}^{\mathsf{T}}, \tag{39}$$

where $n_{\mathrm{e}} = 3(n_{\mathrm{u}} + n_{\mathrm{v}} + n_{\mathrm{w}} + n_{\mathrm{q}}) + n_{\mathrm{h}} + n_{\mathrm{s}}$ is the total number of the nodal DOFs in the element. Next, from Eqs. (38) and (39), it is possible to interpolate the field variables $\{\mathbb{u}, \mathbb{v}, \mathbb{w}, \mathbb{q}, \phi, \psi\}$ in terms of the generalized displacement vector $\mathbb{d}^{\mathrm{e}}$, namely

$$\{\mathbb{u}, \mathbb{v}, \mathbb{w}, \mathbb{q}, \phi, \psi\} = \{\hat{\mathbb{N}}_{\mathrm{u}}, \hat{\mathbb{N}}_{\mathrm{v}}, \hat{\mathbb{N}}_{\mathrm{w}}, \hat{\mathbb{N}}_{\mathrm{q}}, \hat{\mathbb{N}}_{\mathrm{h}}, \hat{\mathbb{N}}_{\mathrm{s}}\}\mathbb{d}^{\mathrm{e}}. \tag{40}$$

As an example, the $3 \times n_{\mathrm{e}}$ matrix $\hat{\mathbb{N}}_{\mathrm{u}}$ is given by

$$\hat{\mathbb{N}}_{\mathrm{u}} = \begin{bmatrix} \mathbb{N}_{\mathrm{u}} & \mathbb{0}_{1\times n_{\mathrm{u}}} & \mathbb{0}_{1\times n_{\mathrm{u}}} & \mathbb{0}_{1\times \hat{n}_{\mathrm{u}}} \\ \mathbb{0}_{1\times n_{\mathrm{u}}} & \mathbb{N}_{\mathrm{u}} & \mathbb{0}_{1\times n_{\mathrm{u}}} & \mathbb{0}_{1\times \hat{n}_{\mathrm{u}}} \\ \mathbb{0}_{1\times n_{\mathrm{u}}} & \mathbb{0}_{1\times n_{\mathrm{u}}} & \mathbb{N}_{\mathrm{u}} & \mathbb{0}_{1\times \hat{n}_{\mathrm{u}}} \end{bmatrix} \quad \text{with} \quad \hat{n}_{\mathrm{u}} = n_{\mathrm{e}} - 3n_{\mathrm{u}}. \tag{41}$$

Combination of Eqs. (2), (13), (26), and (41) leads to the following components for $\delta\mathbf{Y}_{\mathcal{J}}$ $(\mathcal{J} = 0, 1, 2, 3)$:

$$\left.\begin{aligned} \delta Y_{0iI} &= (\hat{\mathbb{N}}_{\mathrm{u}i} N_I + \hat{\mathbb{N}}_{\mathrm{v}i} B_I + \hat{\mathbb{N}}'_{\mathrm{w}i} T_I + \epsilon_{ijk}\Upsilon_{kn} F_{0jI}\hat{\mathbb{N}}_{\mathrm{q}n})\mathbb{d}^{\mathrm{e}} \\ \delta Y_{1iI} &= (2\phi N_I \hat{\mathbb{N}}_{\mathrm{u}i} + T_I \hat{\mathbb{N}}'_{\mathrm{u}i} + \kappa T_I \hat{\mathbb{N}}'_{\mathrm{w}i} + 2n_i N_I \hat{\mathbb{N}}_{\mathrm{h}} + \epsilon_{ijk}\Upsilon_{kn} F_{1jI}\hat{\mathbb{N}}_{\mathrm{q}n})\mathbb{d}^{\mathrm{e}} \\ \delta Y_{2iI} &= (2\psi B_I \hat{\mathbb{N}}_{\mathrm{v}i} + T_I \hat{\mathbb{N}}'_{\mathrm{v}i} + 2b_i B_I \hat{\mathbb{N}}_{\mathrm{s}} + \epsilon_{ijk}\Upsilon_{kn} F_{2jI}\hat{\mathbb{N}}_{\mathrm{q}n})\mathbb{d}^{\mathrm{e}} \\ \delta Y_{3iI} &= (\Upsilon'_{ij}\hat{\mathbb{N}}_{\mathrm{q}j} + \Upsilon_{ij}\hat{\mathbb{N}}'_{\mathrm{q}j})T_I\mathbb{d}^{\mathrm{e}} \end{aligned}\right\}, \tag{42}$$

where $\hat{\mathbb{N}}_{\mathrm{u}i}$ is the i-th row of $\hat{\mathbb{N}}_{\mathrm{u}}$, and the same holds about $\hat{\mathbb{N}}_{\mathrm{v}i}$, $\hat{\mathbb{N}}_{\mathrm{w}i}$, and $\hat{\mathbb{N}}_{\mathrm{q}i}$.

Next, let $\mathbb{A} = \{A_{11}, A_{22}, A_{33}, A_{12}, A_{21}, A_{13}, A_{31}, A_{23}, A_{32}\}^{\mathsf{T}}$ be the vectorial representation of the arbitrary second-order tensor $\mathbf{A}$. From Eq. (42) it is observed that all components of $\delta\mathbf{Y}_{\mathcal{J}}$ $(\mathcal{J} = 0, 1, 2, 3)$ are expressed in terms of the generalized displacement vector $\mathbb{d}^{\mathrm{e}}$. Accordingly, in matrix notation, Eq. (42) may be rewritten as

$$(\delta\mathbb{Y}_{\mathcal{J}})_{9\times 1} = (\hat{\mathbb{B}}_{\mathcal{J}})_{9\times n_{\mathrm{e}}}\mathbb{d}^{\mathrm{e}}_{n_{\mathrm{e}}\times 1}, \quad (\mathcal{J} = 0, 1, 2, 3), \tag{43}$$

where $\delta\mathbb{Y}_{\mathcal{J}}$ is the vectorial representation of $\delta\mathbf{Y}_{\mathcal{J}}$, and the quantities denoted by $\hat{\mathbb{B}}_{\mathcal{J}}$ $(\mathcal{J} = 0, 1, 2, 3)$ may be referred to as the *generalized strain-displacement matrices*. Now, from Eqs. (27), (36), and (43) the expressions for $\delta\mathcal{U}^{\mathrm{e}}$ and $\delta\mathcal{W}^{\mathrm{e}}$ for the typical element take the following simple forms:

$$\delta\mathcal{U}^{\mathrm{e}} = \delta\mathbb{d}^{\mathrm{e}} \cdot \mathbb{F}^{\mathrm{e}}_{\mathrm{int}}, \quad \delta\mathcal{W}^{\mathrm{e}} = \delta\mathbb{d}^{\mathrm{e}} \cdot \mathbb{F}^{\mathrm{e}}_{\mathrm{ext}}, \tag{44}$$

where $\mathbb{F}^{\mathrm{e}}_{\mathrm{int}}$ and $\mathbb{F}_{\mathrm{int}}$ are the internal and external force vectors of the element, respectively. The expression for $\mathbb{F}^{\mathrm{e}}_{\mathrm{int}}$ is given by

$$\mathbb{F}_{\mathrm{int}} = \int_{\mathcal{C}^{\mathrm{e}}} \big(\mathcal{A}\hat{\mathbb{B}}_0^{\mathsf{T}}\mathbb{P}_0 + \mathcal{I}_{\alpha\beta}\hat{\mathbb{B}}_\alpha^{\mathsf{T}}\mathbb{P}_\alpha + \mathcal{I}_{11}^{\star}\hat{\mathbb{B}}_3^{\mathsf{T}}\mathbb{M}_0\big)\mathrm{d}\mathcal{S}, \tag{45}$$

where $\mathbb{P}_{\mathcal{I}}$ ($\mathcal{I} = 0, 1, 2$) and $\mathbb{M}_0$ are the vectorial representations of $\mathbf{P}_{\mathcal{I}}$ and $\mathbf{M}_0$, respectively. Moreover, the external force vector $\mathbb{F}^{\mathrm{e}}_{\mathrm{ext}}$ resulting from a uniform or constant-gradient magnetic loading reads

$$\begin{aligned}\mathbb{F}^{\mathrm{e}}_{\mathrm{ext}} = \frac{1}{\mu_0}\int_{\mathcal{C}^{\mathrm{e}}} \big\{&\mathcal{I}_{11}[(\hat{\mathbb{N}}_{\mathsf{h}}^{\mathsf{T}}\mathbb{n}^{\mathsf{T}} + \boldsymbol{\phi}\hat{\mathbb{N}}_{\mathsf{u}}^{\mathsf{T}})\mathbb{f}_0 + \hat{\mathbb{N}}_{\mathsf{u}}^{\mathsf{T}}\mathbb{f}_1] + \mathcal{I}_{22}[(\hat{\mathbb{N}}_{\mathsf{s}}^{\mathsf{T}}\mathbb{b}^{\mathsf{T}} + \boldsymbol{\psi}\hat{\mathbb{N}}_{\mathsf{v}}^{\mathsf{T}})\mathbb{f}_0 + \hat{\mathbb{N}}_{\mathsf{v}}^{\mathsf{T}}\mathbb{f}_2]\\ &+ \mathcal{I}_{12}(\hat{\mathbb{N}}_{\mathsf{u}}^{\mathsf{T}}\mathbb{f}_2 + \hat{\mathbb{N}}_{\mathsf{v}}^{\mathsf{T}}\mathbb{f}_1) + \mathcal{A}\big(\hat{\mathbb{N}}_{\mathsf{w}}^{\mathsf{T}}\mathbb{f}_0 + \hat{\mathbb{N}}_{\mathsf{q}}^{\mathsf{T}}[(\mathbf{F}_0\tilde{\mathbb{B}}^{\mathrm{rem}}) \times \mathbb{B}^{\mathrm{ext}}]\big)\big\}\mathrm{d}\mathcal{S}.\end{aligned} \tag{46}$$

It is noted that from the virtual work principle and due to arbitrariness of $\delta\mathbb{d}$, a system of nonlinear algebraic equations of the form $\mathbb{F}_{\mathrm{int}} - \mathbb{F}_{\mathrm{ext}} = \mathbb{0}$ is obtained. In this work, the standard Netwon–Raphson method (e.g., Wriggers (2008)) is employed to solve the system of nonlinear equations. Accordingly, let $\Pi^{\mathrm{e}} = \mathcal{U}^{\mathrm{e}} - \mathcal{W}^{\mathrm{e}}$ be the total potential energy of the element. Substituting Eqs. (31), (37), and (44) into the linearized form of the virtual work principle, namely $\Delta\delta\Pi^{\mathrm{e}} = -\delta\Pi^{\mathrm{e}}$, leads to the following system of linear algebraic equations for the increment of the generalized displacement vector $\Delta\mathbb{d}^{\mathrm{e}}$:

$$\mathbb{K}^{\mathrm{e}}\Delta\mathbb{d}^{\mathrm{e}} = -\mathbb{R}^{\mathrm{e}} \quad \text{with} \quad \mathbb{K}^{\mathrm{e}} = \mathbb{K}^{\mathrm{e}}_{\mathrm{mat}} + \mathbb{K}^{\mathrm{e}}_{\mathrm{geo}} - \mathbb{K}^{\mathrm{e}}_{\mathrm{load}} \quad \text{and} \quad \mathbb{R}^{\mathrm{e}} = \mathbb{F}^{\mathrm{e}}_{\mathrm{int}} - \mathbb{F}^{\mathrm{e}}_{\mathrm{ext}}. \tag{47}$$

Here, $\mathbb{K}^{\mathrm{e}}$ and $\mathbb{R}^{\mathrm{e}}$ are the element stiffness matrix and residual vector, respectively. Moreover, $\mathbb{K}^{\mathrm{e}}_{\mathrm{mat}}$, $\mathbb{K}^{\mathrm{e}}_{\mathrm{geo}}$, and $\mathbb{K}^{\mathrm{e}}_{\mathrm{load}}$ are, respectively, the material, geometric, and load part of $\mathbb{K}^{\mathrm{e}}$ with the following components ($\mathcal{I}, \mathcal{J} = 1, 2, ..., n_{\mathrm{e}}$):

$$(\mathbb{K}^{\mathrm{e}}_{\mathrm{mat}})_{\mathcal{I}\mathcal{J}} = \frac{\partial^2(\Delta\delta\mathcal{U}_1)}{\partial(\delta d^{\mathrm{e}}_{\mathcal{I}})\partial(\Delta d^{\mathrm{e}}_{\mathcal{J}})}, \quad (\mathbb{K}^{\mathrm{e}}_{\mathrm{geo}})_{\mathcal{I}\mathcal{J}} = \frac{\partial^2(\Delta\delta\mathcal{U}_2)}{\partial(\delta d^{\mathrm{e}}_{\mathcal{I}})\partial(\Delta d^{\mathrm{e}}_{\mathcal{J}})}, \quad (\mathbb{K}^{\mathrm{e}}_{\mathrm{load}})_{\mathcal{I}\mathcal{J}} = \frac{\partial^2(\Delta\delta\mathcal{W})}{\partial(\delta d^{\mathrm{e}}_{\mathcal{I}})\partial(\Delta d^{\mathrm{e}}_{\mathcal{J}})}. \tag{48}$$

In particular, the material part $\mathbb{K}^{\mathrm{e}}_{\mathrm{mat}}$ may be written in the following simplified form:

$$\mathbb{K}^{\mathrm{e}}_{\mathrm{mat}} = \int_{\mathcal{C}^{\mathrm{e}}} \big[\mathcal{I}_{\alpha\beta}\big(\hat{\mathbb{B}}_0^{\mathsf{T}}\mathbb{D}^1_\alpha\hat{\mathbb{B}}_\beta + \hat{\mathbb{B}}_\alpha^{\mathsf{T}}\mathbb{D}^1_0\hat{\mathbb{B}}_\beta + \hat{\mathbb{B}}_\alpha^{\mathsf{T}}\mathbb{D}^1_\beta\hat{\mathbb{B}}_0\big) + \mathcal{A}\hat{\mathbb{B}}_0^{\mathsf{T}}\mathbb{D}^1_0\hat{\mathbb{B}}_0 + \mathcal{I}_{11}^{\star}\hat{\mathbb{B}}_3^{\mathsf{T}}\mathbb{D}^2\hat{\mathbb{B}}_3\big]\mathrm{d}\mathcal{S}, \tag{49}$$

where $\mathbb{D}^1_{\mathcal{J}}$ ($\mathcal{J} = 0, 1, 2$) and $\mathbb{D}^2$ are the matrix representations of $\boldsymbol{\mathcal{D}}^1_{\mathcal{J}}$ and $\boldsymbol{\mathcal{D}}^2$, respectively. Returning to Eq. (47), the final system of linear algebraic equations is obtained by applying the assembly procedure over all elements in the discretized geometry of the beam. The expressions for the components of the geometric and load part of $\mathbb{K}^{\mathrm{e}}$ are too lengthy and are provided in the Appendix.

6. Numerical examples

In this section, four numerical examples are provided to examine the performance of the developed formulation. A home-written FE code based on the formulation presented in the previous sections has been prepared. For the micropolar beam element employed in the numerical simulations, the number of nodes corresponding to various field variables is considered to be $n^w = n^u = n^v = n^q = n^\phi = n^\psi = 3$. In other words, the element has three nodes and is quadratic in all field variables. Moreover, it is noted that the expression for the Lamé constant λ is given by $\lambda = \frac{\nu}{(1-2\nu)(1+\nu)}E = \frac{2\nu}{(1-2\nu)}\mu$. As usual, E and ν are the Young modulus and Poisson ratio, respectively. For the values of ν close to 0.5, which is observed in HMSMs, the value of λ becomes too large compared to the shear modulus μ. In this case, large values of the terms in the element stiffness matrix containing λ lead to the over-stiffening of the element. In order to alleviate this problem, the selective-reduced integration strategy has been employed in this work. More precisely, for the terms involving λ, the one-point Gauss–Legendre integration rule has been implemented. The rest of the integrals have been evaluated by the three-point integration rule.

6.1. Large deformation of a 45° bend

In this example, an undeformed 45° cantilever curved beam in the x_1x_2 plane is considered. The beam is subjected to a tip shear force along the x_3 direction. This is a well-known benchmark problem that has been investigated in several 3D beam formulations in the context of the classical continuum theory (e.g., Bathe and Bolourchi (1979); Simo and Vu-Quoc (1986); Jelenić and Crisfield (1999); Betsch and Steinmann (2002)). Following Bathe and Bolourchi (1979), the cross-section of the beam is a square of dimension $h = 25.4$ mm, and the initial radius of the arc is $R = 2.54$ m. Additionally, Young modulus and Poisson ratio are $E = 68$ GPa and $\nu = 0$, respectively. Furthermore, the micropolar parameters are considered to be $\eta = k\mu$ and $l = kh$, respectively. Here, k is introduced as a nondimensional parameter.

The problem is solved for several values of $k \in \{0.001, 0.01, 0.07, 0.1, 0.2, 0.3\}$. The maximum load $F = 2664$ N is applied within 12 load steps. To perform convergence analysis, the normalized tip deflection $w_3^T/w_{3\text{conv}}^T$ versus the number of elements is depicted in Fig. 2(a). Here, for each value of the nondimensional parameter k, the converged tip displacement is denoted by $w_{3\text{conv}}^T$. It is observed that even by considering four beam elements, the maximum relative error in deflection, namely $|1 - w_3^T/w_{3\text{conv}}^T|$, is around 0.3%. This shows the excellent convergent properties of the proposed micropolar-based beam element. To have fully converged results, 10 elements are sufficient for all values of k considered in the simulations. The lateral deflection of the beam tip along the x_3 direction vs the nondimensional force $K = FR^2/EI$ is displayed in Fig. 2(b), where $I = h^3/12$ is the cross-sectional moment of inertia. For small values of k, e.g., $k = 0.001$ or $k = 0.01$, the results of the present micropolar formulation are coincident with those reported by Bathe and Bolourchi (1979). However, by increasing the value of k, e.g., for $k = 0.3$ that is equivalent to $l = 0.3h$, the amount of lateral deflection decreases. This indicates that the developed formulation is able to predict

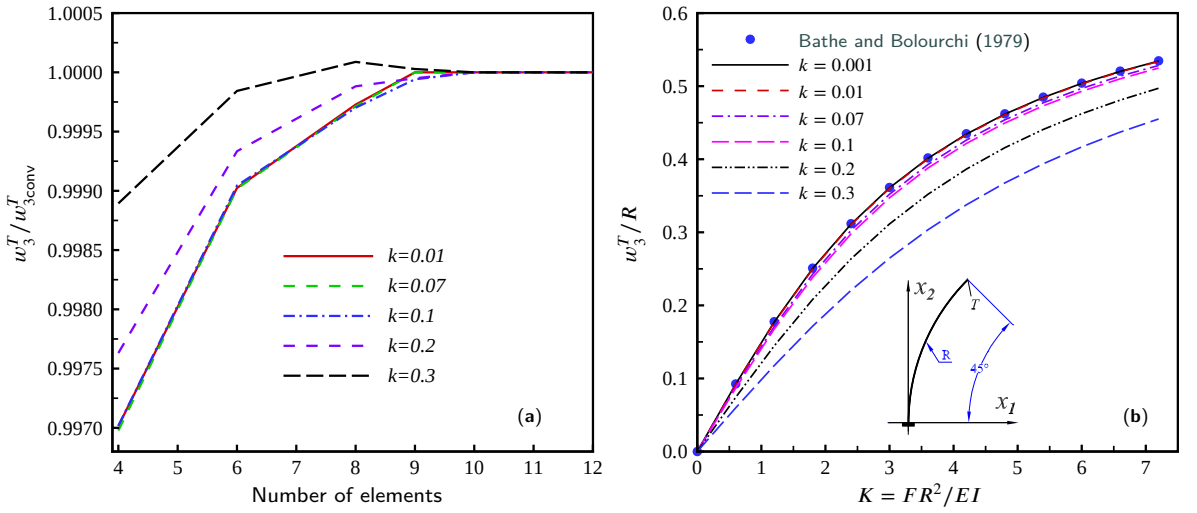

Figure 2: Large deformation of a 45° bend, (**a**): convergence of the tip deflection versus the number of elements, (**b**): deflection-load curves for different values of the nondimensional parameter k

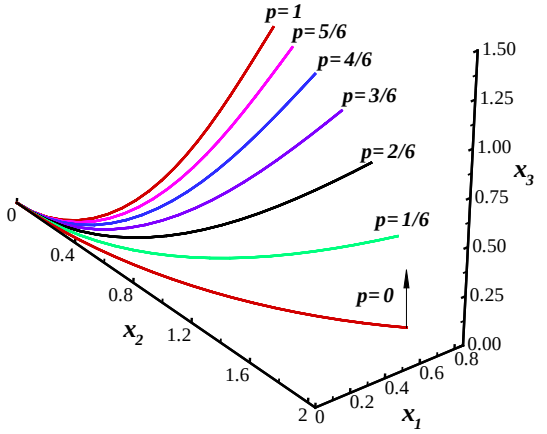

Figure 3: Deformed shapes of the bend for several values of the nondimensional force $p = F/F_{\text{max}}$ (all dimensions in m)

the size-dependent response of beam-like structures when the material length-scale l is comparable with the thickness h. By considering $k = 0.01$, the deformed shapes of the beam for several values of the nondimensional load parameter $p = F/F_{\text{max}}$ are illustrated in Fig. 3.

6.2. Bending of a straight HMS beam

In this example, the two-dimensional deformation of a beam made of HMSMs under a uniform external magnetic flux is investigated. The problem has been experimentally and numerically studied by Yan et al. (2022). The length,

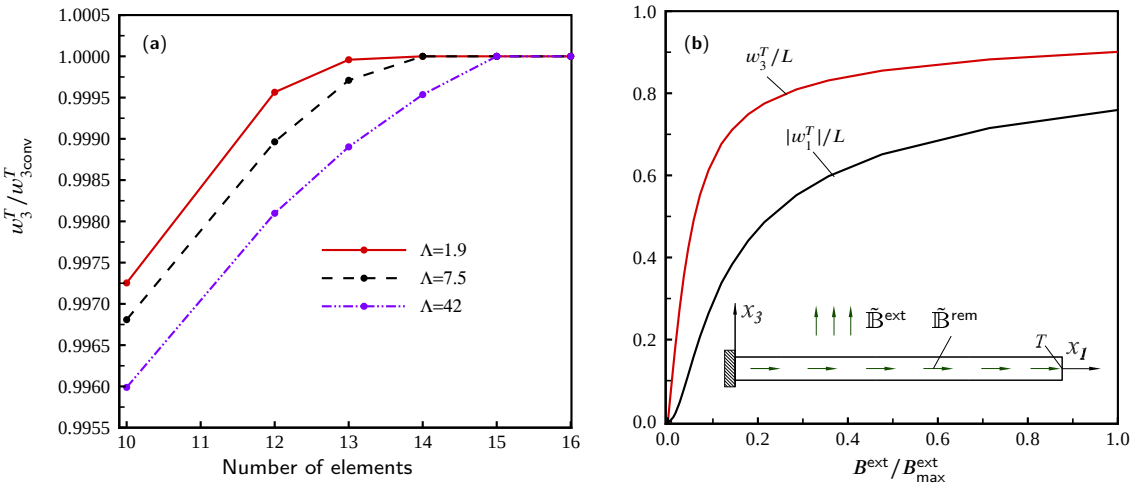

Figure 4: Bending of an HMS beam, (**a**): convergence of the tip deflection versus the number of elements, (**b**): displacement-load curves

width, and thickness of the beam are $L = 13.2$, $w = 1.27$, and $h = 0.5$ mm, respectively. The effective Young modulus of the HMS beam is $E = 1.24$ MPa, and the value of Poisson ratio is $\nu = 0.48$. The remnant magnetic flux vector $\tilde{\mathbb{B}}^{\text{rem}}$ is along the length of the beam, and its corresponding remnant magnetization is $M_0 = \tilde{B}^{\text{rem}}/\mu_0 = 94.1$ KA/m. It is noted that $\tilde{B}^{\text{rem}} = |\tilde{\mathbb{B}}^{\text{rem}}|$ is the magnitude of the remnant magnetic flux vector. Moreover, the micropolar parameters are considered to be $\eta = 0.25\mu$ and $l = 0.25h$. As shown in Fig. 4(a), the uniform magnetic field $\mathbb{B}^{\text{ext}} = B^{\text{ext}}\mathbb{e}_3$ is applied to the beam. The maximum value of the applied magnetic flux is $B^{\text{ext}}_{\text{max}} = 66$ mT. Following Yan et al. (2022), a magneto-elastic nondimensional loading parameter of the form $\Lambda = M_0 B^{\text{ext}} AL^2/EI$ is defined, where $A = wh$ and $I = wh^3/12$ are the cross-sectional area and moment of inertia, respectively. Based on the above-mentioned quantities, the maximum value of the loading parameter is calculated to be $\Lambda_{\text{max}} = 42$. The magnetic loading is applied in 18 load steps, which correspond to $\Lambda \in \{0.2, 0.5, 0.7, 1.1, 1.5, 1.9, 2.4, 3, 3.8, 5, 6, 7.5, 9, 12, 15, 20, 30, 42\}$.

To study the convergence of the numerical solution, the normalized tip deflection $w_3^T/w_{3\text{conv}}^T$ versus the number of elements is displayed in Fig. 4(a). Here, three values for the Λ, namely 1.9, 7.5, and 4.2 have been considered. For each value of Λ, the converged tip deflection is denoted by $w_{3\text{conv}}^T$. As can be seen from the figure, by considering 10 beam elements, the maximum relative error in deflection is around 0.4%. It is also observed that a mesh of 15 elements are needed to have convergent results for all values of Λ. The axial and lateral displacement components of the beam tip vs $B^{\text{ext}}/B^{\text{ext}}_{\text{max}}$ are displayed in Fig. 4(b). In particular, the maximum lateral deflection is obtained to be $w_{3\text{max}}^T = 11.89$ mm. Next, the deformed shapes of the beam for the 18 values of the loading parameter Λ are illustrated in Fig. 5. It is observed that for $\Lambda \in \{0.5, 1.1, 1.9, 3.8, 7.5, 15, 42\}$, the deformed shapes obtained based on the present formulation are very close to those reported by Yan et al. (2022).

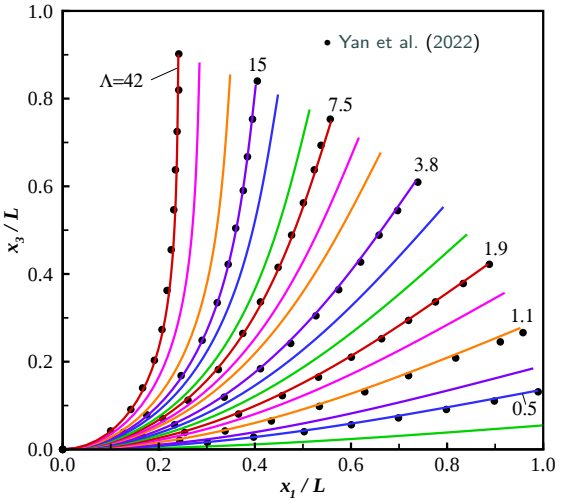

Figure 5: Deformed shapes of the beam for different values of the nondimensional loading parameter $\Lambda \in \{0.2, 0.5, 0.7, 1.1, 1.5, 1.9, 2.4, 3, 3.8, 5, 6, 7.5, 9, 12, 15, 20, 30, 42\}$

6.3. Deformation of helices made of HMSMs under constant-gradient magnetic loading

In this example, the large deformation of three circular helices subjected to a constant-gradient magnetic field is simulated. In Sano et al. (2022), the deformation of three helices having the total lengths $L = 74, 81$, and 103 (mm) have been numerically and experimentally investigated. The geometry of an undeformed helix is displayed in Fig. 6(**a**). If X_3 is the axis of the helix, the undeformed geometry may be described by $X_1 = R\cos\alpha$, $X_2 = R\sin\alpha$, and $X_3 = K\alpha$, with $K = \frac{p}{2\pi}$. Here, α is the polar angle, R is the initial radius, and p is the initial pitch of the helix. In all cases, the helix radius, the wire diameter, and the helix angle are, respectively, considered to be $R = 10$, $d = 2$ (mm), and $\eta = 1.51$ rad. The pitch parameter K is calculated by $K = R\cot\eta$. It is recalled that the relation between the length L and the maximum polar angle $\alpha^{\max}$ is given by $L = Cd\alpha^{\max}$, where $C = \sqrt{R^2 + K^2}$. It is easy to show that the curvature and torsion of the circular helix are constant and are given by $\kappa = R/C^2$ and $\tau = K/C^2$, respectively (e.g., Sahraee and Wriggers (2023)). The effective Young's modulus is $E = 1.32$ (MPa), and Poisson ratio is considered to be $\nu = 0.48$. The remnant magnetic field is directed along the x_3 direction, and its magnitude, in the three helices is $\tilde{B}^{\text{rem}} = 13$, 26 and 13 (mT), respectively. Moreover, the micropolar parameters are considered to be $\eta = 0.1\mu$ and $l = 0.1h$. The helices are clamped at $\alpha = 0$ and are subjected to a constant-gradient magnetic flux of the form expressed in Eq. (34). Following Sano et al. (2022) the nondimensional loading parameter $\Lambda = L(Zb)^{1/3}$, with $Z = A\tilde{B}^{\text{rem}}/(\mu_0 EI)$ is defined. It is noted that A and I are the area and moment of inertia for the circular cross-section of the helices. The maximum value of Λ is considered to be $\Lambda_{\max} = 3.42$ for all the three cases.

For the three helices described above, the normalized tip deflection $w_3^T/w_{3\text{conv}}^T$ versus the number of elements is illustrated in Fig. 6(a). For each helix, the converged tip deflection is denoted by $w_{3\text{conv}}^T$. It is observed that by

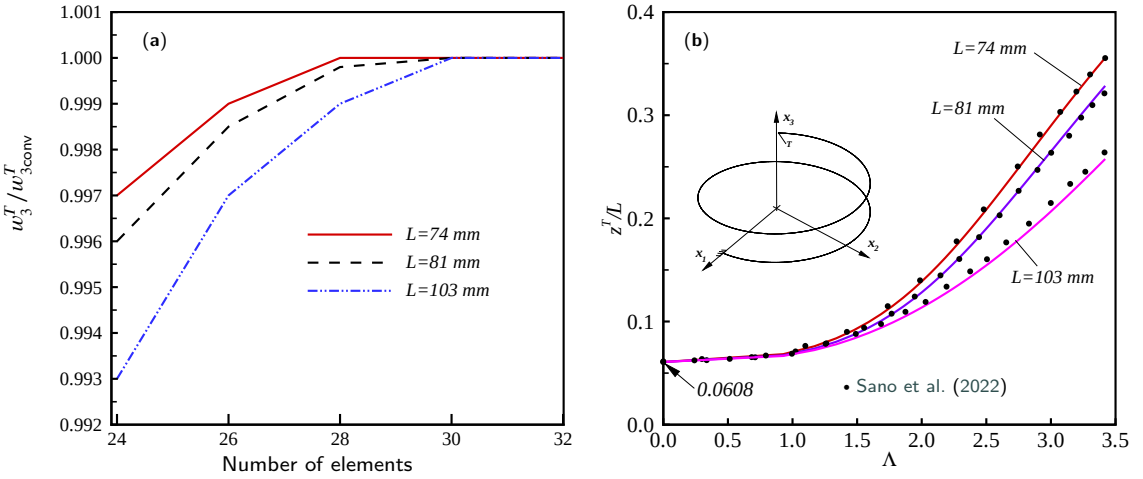

Figure 6: Deformation of the three circular helices under constant-gradient magnetic field, (**a**): convergence of the tip deflection versus the number of elements, (**b**): deflection-load curves

considering 24 beam elements, the maximum relative error in deflection is around 0.7%. However, a mesh of 30 elements are needed to have convergent result in all cases. The nondimensional tip position z^T/L along the x_3-axis vs the nondimensional loading parameter Λ is displayed in Fig. 6(**b**). It is observed that the results based on the present micropolar beam formulation are in good agreement with the data reported by Sano et al. (2022). Moreover, for the helix with $L = 103$ (mm), the three-dimensional deformed shapes and their projection in the $\{x_1x_2, x_2x_3, x_1x_3\}$ planes, for several values of the loading parameter Λ, are demonstrated in Fig. 7(**a**–**d**).

6.4. Deformation of an HMS spiral

In this example, lateral deflection of a spiral-shaped beam under magnetic loading is investigated. The undeformed geometry, displayed in Fig. 8(**a**), is described by the polar equation $r = R + K\alpha$. Here, $R = 1$ and $K = \frac{2}{\pi}$ (cm) are considered. Moreover, α is the polar angle with the maximum value of $\alpha^{\max} = 5\pi$, and the spiral is clamped at $\alpha = \alpha^{\max}$. The remnant magnetic field is assumed to be tangent to the spiral, namely $\tilde{\mathbb{B}}^{\text{rem}} = \tilde{B}^{\text{rem}}\mathbb{T}$, and its magnitude is considered to be $\tilde{B}^{\text{rem}} = 13$ (mT). The values of wire diameter, effective Young modulus, and Poisson ratio are considered to be $d = 2$ (mm), $E = 1.32$ MPa, and $\nu = 0.48$, respectively. Moreover, the micropolar parameters are $\eta = 0.1\mu$ and $l = 0.1h$.

The spiral is subjected to the constant magnetic field in the x_3 direction, giving $\mathbb{B}^{\text{ext}} = B^{\text{ext}}\mathbb{e}_3$. The maximum value of the applied magnetic field is $B^{\text{ext}}_{\max} = 30$ mT, and the maximum load is applied in 60 load steps.

The normalized tip deflection $w_3^T / w_{3\text{conv}}^T$ versus the number of elements is displayed in Fig. 8(a). Here, $w_{3\text{conv}}^T$ is the converged tip deflection of the spiral. It observed from the figure that by considering 50 beam elements, the

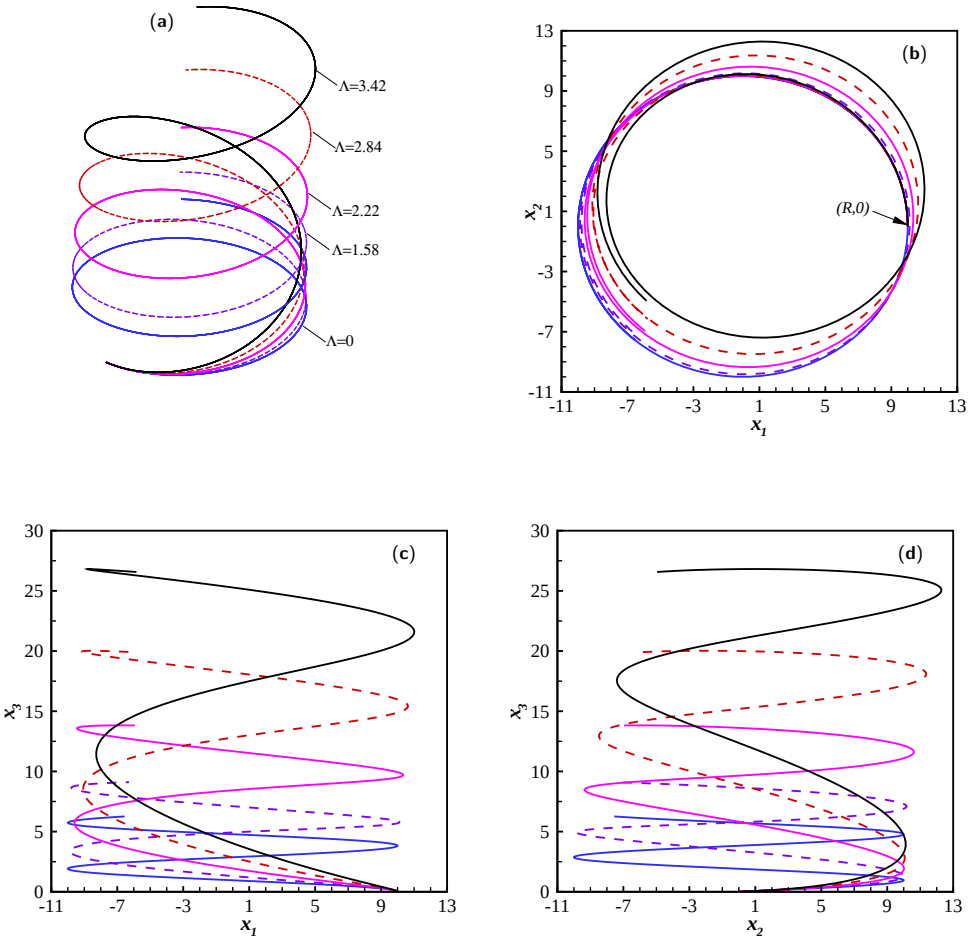

Figure 7: Deformed shapes of the helix with $L = 103$ mm in the 3D space (**a**) and in the $\{x_1x_2, x_2x_3, x_1x_3\}$ projection planes (**b–d**) for $\Lambda \in \{1.58, 2.22, 2.84, 3.42\}$

relative error in tip deflection is around 1%. However, by considering a mesh of 60 elements, a convergent result is achieved. The displacement components of the spiral tip against the nondimensional parameter $\frac{1}{\mu\mu_0}\tilde{B}^{\text{rem}}B^{\text{ext}} \times 10^4$ are plotted in Fig. 8(**b**). The maximum lateral deflection, at the tip of the spiral, is obtained to be $w^T_{3\text{max}} = 6.78$ (cm). Finally, three-dimensional deformed shapes of the beam and their projection in the $\{x_1x_2, x_2x_3, x_1x_3\}$ planes, for $B^{\text{ext}} \in \{10, 20, 30\}$ mT, are illustrated in Fig. 9(**a–d**).

7. Summary

In this work, a nonlinear beam model based on the micropolar continuum theory was developed. The undeformed beams may have 3D geometries with arbitrary initial curvature and torsion. The kinematic quantities were described based on the motion of the centreline, deformation of two lateral directors, and micro-rotation of the beam cross-section.

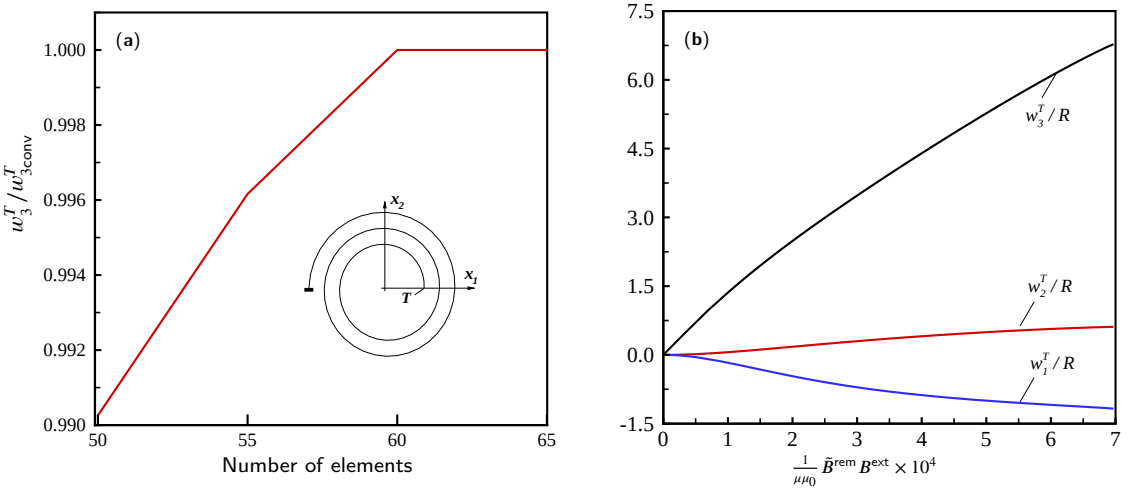

Figure 8: A spiral under magnetic loading, (**a**): convergence of the tip deflection versus the number of elements, (**b**): deflection-load curves

Three-dimensional constitutive equations can be directly used in the proposed formulation. From the application point of view, it was indicated that the proposed formulation can model the deformation of smart beams made of HMSMs. In this regard, the virtual external loading was formulated so that a uniform or constant-gradient external magnetic flux can be applied to the present beam model. Additionally, a nonlinear FE formulation in the material framework was developed to provide numerical solutions in various geometries and loading conditions. Numerical examples indicate that the present beam model may have two specific applications in engineering designs. The first application is to capture the well-known size effect phenomenon if the material length-scale parameter of the micropolar theory is comparable with the beam thickness. The second one is to model the deformation of beam-like structures made of HMSMs and subject to magnetic loading. In this case, it was shown that the results of the present formulation are in excellent agreement with those available in the literature.

Declaration of competing interest

The authors declare no competing interests.

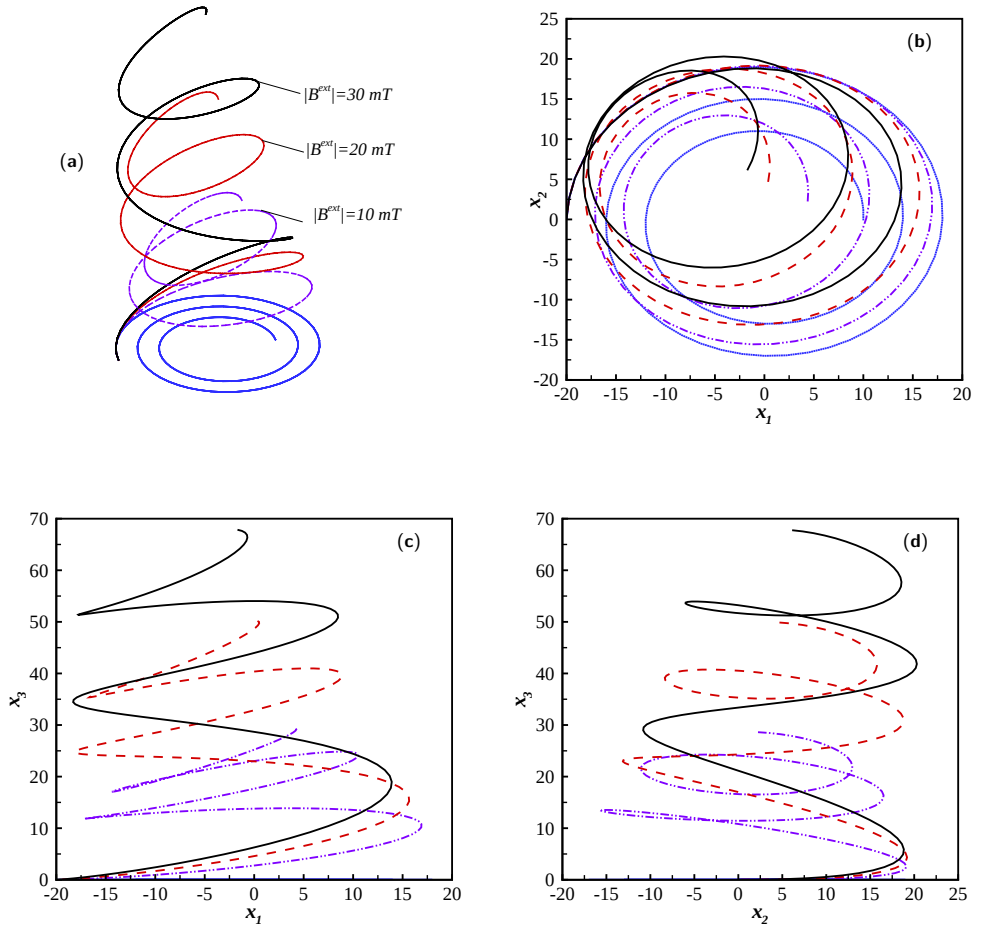

Figure 9: Deformed shapes in the 3D space (**a**) and in the $\{x_1x_2, x_2x_3, x_1x_3\}$ projection planes (**b–d**) for $B^{\text{ext}} \in \{10, 20, 30\}$ mT

Appendix

In this appendix, the expressions for the components of $\mathbb{K}^{\text{e}}_{\text{geo}}$ and $\mathbb{K}_{\text{load}}$ are presented. From Eqs. $(31)_2$, (40), and $(48)_2$ the expression for $(\mathbb{K}^{\text{e}}_{\text{geo}})_{\mathcal{IJ}}$, with $\mathcal{I}, \mathcal{J} = 1, 2, ..., n_{\text{e}}$, may be written as follows:

$$(\mathbb{K}^{\text{e}}_{\text{geo}})_{\mathcal{IJ}} = \int_C \big[\mathcal{I}_{\alpha\beta} P_{\alpha ij}(H_{in\mathcal{IJ}} F_{\alpha nj} + H^{\alpha}_{ij\mathcal{IJ}} + H^{\alpha}_{ij\mathcal{JI}}) + \mathcal{I}^{\star}_{11} M_{0ij} T_j H^3_{i\mathcal{IJ}} + \mathcal{A} P_{0ij}(H_{in\mathcal{IJ}} F_{0nj} + H^{0}_{ij\mathcal{IJ}} + H^{0}_{ij\mathcal{JI}})\big] \mathrm{d}S, \tag{A-1}$$

where the quantities denoted by $H_{in\mathcal{IJ}}$ and $H^3_{i\mathcal{IJ}}$ are calculated to be

$$H_{in\mathcal{IJ}} = (\epsilon_{inp}\Upsilon_{par} + \Upsilon_{nr}\Upsilon_{ia} - \Upsilon_{tr}\Upsilon_{ta})\hat{N}_{\mathrm{q}a\mathcal{I}}\hat{N}_{\mathrm{q}r\mathcal{J}}, \tag{A-2}$$

$$
\begin{aligned}
H^3_{i\mathcal{I}\mathcal{J}} =& (\Upsilon_{imrs} q'_s \hat{N}_{\mathsf{q}r\mathcal{J}} + \Upsilon_{imr} \hat{N}'_{\mathsf{q}r\mathcal{J}}) \hat{N}_{\mathsf{q}m\mathcal{I}} + \Upsilon_{imr} \hat{N}'_{\mathsf{q}m\mathcal{I}} \hat{N}_{\mathsf{q}r\mathcal{J}} \\
&+ (\Upsilon_{mrs} q'_s \hat{N}_{\mathsf{q}r\mathcal{I}} + \Upsilon_{mr} \hat{N}'_{\mathsf{q}r\mathcal{I}}) \epsilon_{imn} \Upsilon_{nt} \hat{N}_{\mathsf{q}t\mathcal{J}}.
\end{aligned}
\tag{A-3}
$$

Moreover, the quantities shown by $H^{\mathcal{K}}_{ij\mathcal{I}\mathcal{J}}$ ($\mathcal{K} = 0, 1, 2$) may be written as $H^{\mathcal{K}}_{ij\mathcal{I}\mathcal{J}} = \epsilon_{imn} \Upsilon_{nr} \hat{N}_{\mathsf{q}r\mathcal{I}} F^{\mathcal{K}}_{jm\mathcal{J}}$, with

$$
\left.
\begin{aligned}
F^0_{jm\mathcal{J}} &= N_j \hat{N}_{\mathsf{u}m\mathcal{J}} + B_j \hat{N}_{\mathsf{v}m\mathcal{J}} + T_j \hat{N}'_{\mathsf{w}m\mathcal{J}} \\
F^1_{jm\mathcal{J}} &= 2N_j (n_m \hat{N}_{\mathsf{h}\mathcal{J}} + \phi \hat{N}_{\mathsf{u}m\mathcal{J}}) + T_j (\kappa \hat{N}'_{\mathsf{w}m\mathcal{J}} - \tau \hat{N}_{\mathsf{v}m\mathcal{J}} + \hat{N}'_{\mathsf{u}m\mathcal{J}}) \\
F^2_{jm\mathcal{J}} &= 2B_j (b_m \hat{N}_{\mathsf{s}\mathcal{J}} + \psi \hat{N}_{\mathsf{v}m\mathcal{J}}) + T_j (\hat{N}'_{\mathsf{v}m\mathcal{J}} + \tau \hat{N}_{\mathsf{u}m\mathcal{J}})
\end{aligned}
\right\}.
\tag{A-4}
$$

It is noted that $F_{\alpha ij}$, $P_{\alpha ij}$, and $\hat{N}_{\mathsf{u}i\mathcal{I}}$ are the components of $\mathbf{F}_\alpha$, $\mathbf{P}_\alpha$, and $\hat{\mathbb{N}}_{\mathsf{u}}$, respectively. The same holds for similar quantities present in the above equations. Moreover, $\Upsilon_{ijk} = \partial \Upsilon_{ij} / \partial q_k$ and $\Upsilon_{ijkl} = \partial^2 \Upsilon_{ij} / \partial q_k \partial q_l$ are the partial derivatives of Υ_{ij} with respect to the micro-rotation components. To calculate the components of the load stiffness matrix $\mathbb{K}^{\mathrm{e}}_{\mathrm{geo}}$, from Eqs. (37), (40), and $(48)_3$ it follows that

$$
\begin{aligned}
(\mathbb{K}^{\mathrm{e}}_{\mathrm{load}})_{\mathcal{I}\mathcal{J}} = \int_C \Big\{ & G^{\mathrm{ext}}_{im} \tilde{B}^{\mathrm{rem}}_n \big[\mathcal{I}_{11} \big((n_i \hat{N}_{\mathsf{h}\mathcal{I}} + \phi \hat{N}_{\mathsf{u}i\mathcal{I}}) F^0_{mnJ} + \hat{N}_{\mathsf{u}i\mathcal{I}} F^1_{mnJ} \big) \\
& + \mathcal{I}_{22} \big((b_i \hat{N}_{\mathsf{s}\mathcal{I}} + \psi \hat{N}_{\mathsf{v}i\mathcal{I}}) F^0_{mnJ} + \hat{N}_{\mathsf{v}i\mathcal{I}} F^2_{mnJ} \big) \\
& + \mathcal{I}_{12} (\hat{N}_{\mathsf{u}i\mathcal{I}} F^2_{mnJ} + \hat{N}_{\mathsf{v}i\mathcal{I}} F^1_{mnJ}) + \mathcal{A} \hat{N}_{\mathsf{w}i\mathcal{I}} F^0_{mnJ} \big] \\
& + f_{0i} \big[\mathcal{I}_{11} (\hat{N}_{\mathsf{h}\mathcal{I}} \hat{N}_{\mathsf{u}i\mathcal{J}} + \hat{N}_{\mathsf{h}\mathcal{J}} \hat{N}_{\mathsf{u}i\mathcal{I}}) + \mathcal{I}_{22} (\hat{N}_{\mathsf{s}\mathcal{I}} \hat{N}_{\mathsf{v}i\mathcal{J}} + \hat{N}_{\mathsf{s}\mathcal{J}} \hat{N}_{\mathsf{v}i\mathcal{I}}) \big] \\
& + \mathcal{A} \tilde{B}^{\mathrm{rem}}_n B^{\mathrm{ext}}_r \epsilon_{mri} \hat{N}_{\mathsf{q}i\mathcal{I}} F^0_{mnJ} \Big\} \mathrm{d}S.
\end{aligned}
\tag{A-5}
$$

References

Abadikhah, H., Folkow, P.D., 2015. A hierarchy of dynamic equations for micropolar plates. Journal of Sound and Vibration 357, 427–436.

Bastola, A., Hossain, M., 2021. The shape-morphing performance of magnetoactive soft materials. Materials & Design 211, 110172.

Bathe, K.J., Bolourchi, S., 1979. Large displacement analysis of three-dimensional beam structures. International Journal for Numerical Methods in Engineering 14, 961–986.

Bauer, S., Dettmer, W., Peric, D., Schäfer, M., 2012a. Micropolar hyper-elasticity: constitutive model, consistent linearization and simulation of 3d scale effects. Computational Mechanics 50, 383–396.

Bauer, S., Dettmer, W., Peric, D., Schäfer, M., 2012b. Micropolar hyper-elastoplasticity: constitutive model, consistent linearization, and simulation of 3d scale effects. International Journal for Numerical Methods in Engineering 91, 39–66.

Bauer, S., Schäfer, M., Grammenoudis, P., C., T., 2010. Three-dimensional finite elements for large deformation micropolar elasticity. Computer Methods in Applied Mechanics and Engineering 199, 2643–2654.

Betsch, P., Steinmann, P., 2002. Frame-indifferent beam finite elements based upon the geometrically exact beam theory. International journal for numerical methods in engineering 54, 1775–1788.

de Borst, R., 1993. A generalisation of J2-flow theory for polar continua. Computer Methods in Applied Mechanics and Engineering 103, 347–362.

Chen, W., Wang, L., Yan, Z., Luo, B., 2021. Three-dimensional large-deformation model of hard-magnetic soft beams. Composite Structures 266, 113822.

Chowdhury, S., Reddy, J., 2019. Geometrically exact micropolar Timoshenko beam and its application in modelling sandwich beams made of architected lattice core. Composite Structures 226, 111228.

Cui, Z., Yuan, Z., Ju, J., 2023. Mechanical couplings of 3d lattice materials discovered by micropolar elasticity and geometric symmetry. Journal of Applied Mechanics 90, 041001.

Dadgar-Rad, F., Hossain, M., 2022a. Finite deformation analysis of hard-magnetic soft materials based on micropolar continuum theory. International Journal of Solids and Structures 251, 111747.

Dadgar-Rad, F., Hossain, M., 2022b. Large viscoelastic deformation of hard-magnetic soft beams. Extreme Mechanics Letters 54, 101773.

Dadgar-Rad, F., Hossain, M., 2023. A micropolar shell model for hard-magnetic soft materials. International Journal for Numerical Methods in Engineering 124, 1798–1817.

Dorfmann, L., Ogden, R.W., 2014. Nonlinear Theory of Electroelastic and Magnetoelastic Interactions. Springer.

Erdelj, S., Jelenić, G., Ibrahimbegović, A., 2020. Geometrically non-linear 3d finite-element analysis of micropolar continuum. International Journal of Solids and Structures 202, 745–764.

Eremeyev, V., Altenbach, H., 2017. Basics of mechanics of micropolar shells. Shell-like Structures: Advanced Theories and Applications , 63–111.

Eringen, A.C., 1966. Mechanics of micromorphic materials, in: Applied Mechanics: Proceedings of the Eleventh International Congress of Applied Mechanics Munich (Germany) 1964, Springer. pp. 131–138.

Eringen, A.C., 1999. Microcontinuum Field Theories: I. Foundations and Solids. Springer.

Eringen, A.C., Edelen, D., 1972. On nonlocal elasticity. International journal of engineering science 10, 233–248.

Eringen, A.C., Kafadar, C.B., 1976. Polar field theories, in: Eringen, A.C. (Ed.), Continuum Physics, vol IV. Elsevier, pp. 1–73.

Fares, M., Salem, M., Atta, D., Elmarghany, M.K., 2023. Mixed variational principle for micropolar elasticity and an accurate two-dimensional plate model. European Journal of Mechanics - A/Solids 99, 104870.

Garcia-Gonzalez, D., 2019. Magneto-visco-hyperelasticity for hard-magnetic soft materials: theory and numerical applications. Smart Materials and Structures 28, 085020.

Garcia-Gonzalez, D., Hossain, M., 2021a. A microstructural-based approach to model magneto-viscoelastic materials at finite strains. International Journal of Solids and Structures 208–209, 119–132.

Garcia-Gonzalez, D., Hossain, M., 2021b. Microstructural modelling of hard-magnetic soft materials: Dipole–dipole interactions versus zeeman effect. Extreme Mechanics Letters 48, 101382.

Goda, I., Assidi, M., Ganghoffer, G., 2014. A 3d elastic micropolar model of vertebral trabecular bone from lattice homogenization of the bone microstructure. Biomechanics and Modeling in Mechanobiology 13, 53–83.

Grammenoudis, P., Sator, C., Tsakmakis, C., 2007. Micropolar plasticity theories and their classical limits. Part II: Comparison of responses predicted by the limiting and a standard classical model. Acta Mechanica 189, 177–191.

Grammenoudis, P., Tsakmakis, C., 2007. Micropolar plasticity theories and their classical limits, Part I: Resulting model. Acta Mechanica 189, 151–175.

Guarín-Zapata, N., Gomez, J., Valencia, C., Dargush, G., Hadjesfandiari, A., 2020. Finite element modeling of micropolar-based phononic crystals. Wave Motion 92, 102406.

Hassanpour, S., Heppler, G., 2016. Comprehensive and easy-to-use torsion and bending theories for micropolar beams. International Journal of Mechanical Sciences 114, 71–87.

Jelenić, G., Crisfield, M., 1999. Geometrically exact 3d beam theory: implementation of a strain-invariant finite element for statics and dynamics. Computer methods in applied mechanics and engineering 171, 141–171.

Kafadar, C., Eringen, A., 1971. Micropolar media–I The classical theory. International Journal of Engineering Science 9, 271–307.

Kim, Y., Yuk, H., Zhao, R., Chester, S., Zhao, X., 2018. Printing ferromagnetic domains for untethered fast-transforming soft materials. Nature 558, 274–279.

Kuang, X., Wu, S., Ze, Q., Yue, L., Jin, Y., Montgomery, S., Yang, F., Qi, H., Zhao, R., 2019. Magnetic dynamic polymers for modular assembling and reconfigurable morphing architectures. Advanced Materials , 2102113.

La Valle, G., Falsone, G., 2023. Random micropolar beams: response and identification. International Journal of Non-Linear Mechanics 150, 104367.

Lam, D.C., Yang, F., Chong, A., Wang, J., Tong, P., 2003. Experiments and theory in strain gradient elasticity. Journal of the Mechanics and Physics of Solids 51, 1477–1508.

Li, X., Yu, W., Liu, J., Zhu, X., Wang, H., Sun, X., Liu, J., Yuan, H., 2023. A mechanics model of hard-magnetic soft rod with deformable cross-section under three-dimensional large deformation. International Journal of Solids and Structures 279, 112344.

Liu, J., Yang, Y., Li, M., Xu, F., 2023. A meshfree model of hard-magnetic soft materials. International Journal of Mechanical Sciences 258, 108566.

Lucarini, S., Hossain, M., Garcia-Gonzalez, D., 2022. Recent advances in hard-magnetic soft composites: synthesis, characterisation, computational modelling, and applications. Composite Structures 200, 210001.

Mayeur, J., McDowell, D., Bammann, D., 2011. Dislocation-based micropolar single crystal plasticity: Comparison of multi- and single criterion theories. Journal of the Mechanics and Physics of Solids 59, 398–422.

McFarland, A.W., Colton, J.S., 2005. Role of material microstructure in plate stiffness with relevance to microcantilever sensors. Journal of Micromechanics and Microengineering 15, 1060.

Mindlin, R.D., 1965. Second gradient of strain and surface-tension in linear elasticity. International Journal of Solids and Structures 1, 417–438.

Moreno-Mateos, M.A., Danas, K., Garcia-Gonzalez, D., 2023. Influence of magnetic boundary conditions on the quantitative modelling of magnetorheological elastomers. Mechanics of Materials 184, 104742.

Mukherjee, D., Rambausek, M., Danas, K., 2021. An explicit dissipative model for isotropic hard magnetorheological elastomers. Journal of the Mechanics and Physics of Solids 151, 104361.

Narayanan, P., Pramanik, R., Arockiarajan, A., 2023. Micromechanics-based constitutive modeling of hard-magnetic soft materials. Mechanics of Materials , 104722.

Obrezkov, L., Matikainen, M.K., Kouhia, R., 2022. Micropolar beam-like structures under large deformation. International Journal of Solids and Structures 254-255, 111899.

Pietraszkiewicz, W., Eremeyev, V., 2009. On natural strain measures of the non-linear micropolar continuum. International Journal of Solids and Structures 46, 774–787.

Rajan, A., Arockiarajan, A., 2021. Bending of hard-magnetic soft beams: A finite elasticity approach with anticlastic bending. European Journal of Mechanics A/Solids 90, 104374.

Ramezani, S., Naghdabadi, R., Sohrabpour, S., 2008. Non-linear finite element implementation of micropolar hypo-elastic materials. Computer Methods in Applied Mechanics and Engineering 197, 4149–4159.

Ramezani, S., Naghdabadi, R., Sohrabpour, S., 2009a. Analysis of micropolar elastic beams. European Journal of Mechanics-A/Solids 28, 202–208.

Ramezani, S., Naghdabadi, R., Sohrabpour, S., 2009b. Constitutive equations for micropolar hyper-elastic materials. International Journal of Solids and Structures 46, 2765–2773.

Ren, Z., Hu, W., Dong, X., Sitti, M., 2019. Multi-functional soft-bodied jellyfish-like swimming. Nature communications 10, 2703.

Saber, A., Sedaghati, R., 2023. On the modeling of magnetorheological elastomers: A state-of-the-art review. Advanced Engineering Materials 25, 2300182.

Sahraee, S., Wriggers, P., 2023. Tensor Calculus and Differential Geometry for Engineers: With Solved Exercises. Springer.

Sano, T.G., Pezzulla, M., Reis, P.M., 2022. A Kirchhoff-like theory for hard magnetic rods under geometrically nonlinear deformation in three dimensions. Journal of the Mechanics and Physics of Solids 160, 104739.

Sansour, C., 1998. Large strain deformations of elastic shells constitutive modelling and finite element analysis. Computer Methods in Applied Mechanics and Engineering 161, 1–18.

Sargsyan, S., Khachatryan, M., 2022. Construction of a bending model of micropolar elastic thin beams with a circular axis and its implementation using the finite element method. Journal of Applied Mechanics and Technical Physics 63, 1205–1217.

Simo, J.C., Vu-Quoc, L., 1986. A three-dimensional finite-strain rod model. part ii: Computational aspects. Computer methods in applied mechanics and engineering 58, 79–116.

Spadoni, A., Ruzzene, M., 2012. Elasto-static micropolar behavior of a chiral auxetic lattice. Journal of the Mechanics and Physics of Solids 60, 156–171.

Steinmann, P., 1994. A micropolar theory of finite deformation and finite rotation multiplicative elastoplasticity. International Journal of Solids and Structures 31, 1063–1084.

Stewart, E.M., Anand, L., 2023. Magneto-viscoelasticity of hard-magnetic soft-elastomers: Application to modeling the dynamic snap-through behavior of a bistable arch. Journal of the Mechanics and Physics of Solids , 105366.

Suh, S., Sun, W.C., O'Connor, D., 2020. A phase field model for cohesive fracture in micropolar continua. Computer Methods in Applied Mechanics and Engineering 369, 113181.

Tian, J., Lai, Y., Liu, E., He, C., 2023. A thermodynamics-based micro-macro elastoplastic micropolar continuum model for granular materials. Computers and Geotechnics 162, 105653.

Truesdell, C., Noll, W., 2004. The Non-Linear Field Theories of Mechanics. Springer.

Voyiadjis, G.Z., Song, Y., 2019. Strain gradient continuum plasticity theories: theoretical, numerical and experimental investigations. International Journal of Plasticity 121, 21–75.

Wan, J., Yang, D., Chu, X., Qu, W., 2022. A micropolar peridynamic differential operator and simulation of crack propagation. Engineering Fracture Mechanics 269, 108532.

Wang, L., Kim, Y., Guo, G., Zhao, X., 2020. Hard-magnetic elastica. Journal of the Mechanics and Physics of Solids 142, 104045.

Wang, L., Zheng, D., Harker, P., Patel, A.B., Guo, C.F., Zhao, X., 2021. Evolutionary design of magnetic soft continuum robots. Proceedings of the National Academy of Sciences 118, e2021922118.

Wriggers, P., 2008.

Wu, S., Hamel, C., Ze, Q., Yang, F., Qi, H., Zhao, R., 2021. Evolutionary algorithm-guided voxel-encoding printing of functional hard-magnetic soft active materials. Advanced Intelligent Systems 2, 2000060.

Wu, S., Hu, W., Ze, Q., Sitti, M., Zhao, R., 2020. Multifunctional magnetic soft composites: a review. Multifunctional Materials 3, 042003.

Yan, D., Abbasi, A., Reis, P.M., 2022. A comprehensive framework for hard-magnetic beams: reduced-order theory, 3d simulations, and experiments. International Journal of Solids and Structures 257, 111319.

Yan, D., Aymon, B.F., Reis, P.M., 2023. A reduced-order, rotation-based model for thin hard-magnetic plates. Journal of the Mechanics and Physics of Solids 170, 105095.

Ye, H., Li, Y., Zhang, T., 2021. Magttice: A lattice model for hard-magnetic soft materials. Soft Matter 17, 3560–3568.

Yoder, M., Thompson, L., Summers, J., 2018. Size effects in lattice structures and a comparison to micropolar elasticity. International Journal of Solids and Structures 143, 245–261.

Zhang, R., Wu, S., Ze, Q., Zhao, R., 2020. Micromechanics study on actuation efficiency of hard-magnetic soft active materials. Journal of Applied Mechanics 87, 091008.

Zhao, R., Kim, Y., Chester, A., Sharma, P., Zhao, X., 2019. Mechanics of hard-magnetic soft materials. Journal of the Mechanics and Physics of Solids 124, 244–263.

Zozulya, V., 2018. Higher order theory of micropolar plates and shells. Journal of Applied Mathematics and Mechanics (ZAMM) 98, 886–918.